



Discovery of 21 New Changing-look AGNs in the Northern Sky

Qian Yang^{1,2} , Xue-Bing Wu^{1,2} , Xiaohui Fan^{2,3} , Linhua Jiang² , Ian McGreer³ , Jinyi Shangguan^{1,2} , Su Yao²,
Bingquan Wang¹, Ravi Joshi², Richard Green³, Feige Wang^{1,2} , Xiaotong Feng^{1,2},
Yuming Fu^{1,2}, Jinyi Yang^{1,2} , and Yuanqi Liu¹

¹ Department of Astronomy, School of Physics, Peking University, Beijing 100871, People's Republic of China; qianyang.astro@pku.edu.cn

² Kavli Institute for Astronomy and Astrophysics, Peking University, Beijing 100871, People's Republic of China

³ Steward Observatory, University of Arizona, 933 North Cherry Avenue, Tucson, AZ 85721, USA

Received 2017 November 21; revised 2018 May 18; accepted 2018 June 2; published 2018 July 27

Abstract

The rare case of changing-look (CL) active galactic nuclei (AGNs), with the appearance or disappearance of broad Balmer emission lines within a few years, challenges our understanding of the AGN unified model. We present a sample of 21 new CL AGNs at $0.08 < z < 0.58$, which doubles the number of such objects known to date. These new CL AGNs were discovered in various ways, from (1) repeat spectra in the SDSS, (2) repeat spectra in the Large Sky Area Multi-Object Fiber Spectroscopic Telescope (LAMOST) and SDSS, and (3) photometric variability and new spectroscopic observations. We use the photometric data from surveys, including the SDSS imaging survey, the Pan-STARRS1, the DESI Legacy imaging survey, the *Wide-field Infrared Survey Explorer* (WISE), the Catalina Real-time Transient Survey, and the Palomar Transient Factory. The estimated upper limits of the transition timescale of the CL AGNs in this sample spans from 0.9 to 13 years in the rest-frame. The continuum flux in the optical and mid-infrared becomes brighter when the CL AGNs turn on, or vice versa. Variations of more than 0.2 mag in the W1 band were detected in 15 CL AGNs during the transition. The optical and mid-infrared variability is not consistent with the scenario of variable obscuration in 10 CL AGNs at more than the 3σ confidence level. We confirm a bluer-when-brighter trend in the optical. However, the mid-infrared WISE colors W1–W2 become redder when the objects become brighter in the W1 band, possibly due to a stronger hot dust contribution in the W2 band when the AGN activity becomes stronger. The physical mechanism of type transition is important for understanding the evolution of AGNs.

Key words: black hole physics – galaxies: active – galaxies: nuclei

1. Introduction

Active galactic nuclei (AGNs) are classified into Type 1 and Type 2 AGNs based on their emission-line features (e.g., Seyfert 1943; Khachikian & Weedman 1971). Type 1 AGNs show broad ($1000\text{--}20,000\text{ km s}^{-1}$) and narrow ($300\text{--}1000\text{ km s}^{-1}$) emission lines, while only narrow emission lines are present in Type 2 AGNs (Netzer 2015, and references therein). This dichotomy is explained in the unified model (Antonucci 1993; Urry & Padovani 1995) as a viewing angle effect due to the obscuration of the broad-line region (BLR). Intermediate AGN types exist. Type 1.8 (1.9) is classified by a broad H α and a weak (absent) broad H β line (Osterbrock 1981). Type 1.5 is an intermediate type between Type 1 and Type 2 with an apparent narrow H β profile superimposed on broad H β components (Osterbrock & Koski 1976; Osterbrock 1977). The intermediate type objects are explained as Type 2 objects observed in scattered light (Antonucci & Miller 1985), or partial obscuration by optically thin dust (Stern & Laor 2012). An alternative scenario is that the different classes are evolutionary (Penston & Perez 1984; Korista & Goad 2004; Wang & Zhang 2007; Elitzur et al. 2014). Penston & Perez (1984) proposed that the Type 2 class AGNs are possibly Type 1 AGNs in which the continuum source is temporarily off.

Some AGNs were observed to change between different spectral types; these are the so-called changing-look (CL) AGNs. The term “changing-look” was originally used in X-rays, in which objects were found to change from Compton-thick to Compton-thin, or vice versa (e.g., Matt et al. 2003;

Bianchi et al. 2005; Piconcelli et al. 2007; Ballo et al. 2008; Risaliti et al. 2009; Marchese et al. 2012; Ricci et al. 2016). Lately, this term has been widened to describe objects with optical spectral type transitions (e.g., Denney et al. 2014; LaMassa et al. 2015; MacLeod et al. 2016; McElroy et al. 2016; Ruan et al. 2016; Runnoe et al. 2016; Gezari et al. 2017). The physical mechanisms of the changes are still under debate. The main plausible mechanisms are (1) variable obscuration due to the movement of obscuring material, in a scenario in which the dusty toroidal structure obscuring the BLR has a patchy distribution (e.g., Nenkova et al. 2008a, 2008b; Elitzur 2012) or an accelerating outflow (e.g., Shapovalova et al. 2010); (2) variable accretion rate, in an evolutionary paradigm in which an AGN follows an evolutionary sequence from Type 1 to intermediate type and later to Type 2, or vice versa (e.g., Penston & Perez 1984; Elitzur et al. 2014); or (3) a tidal disruption event (TDE) of a star disrupted by the supermassive black hole (SMBH), which may also result in a change of classification (Eracleous et al. 1995; Merloni et al. 2015; Blanchard et al. 2017). The nature of the type transition is important for understanding the evolution of AGNs.

Spectral type changes, with the appearance or disappearance of broad Balmer emission lines, have been detected in only a small number of AGNs. Long-timescale observations of a handful of AGNs show that some AGNs have changed from Type 1 to Type 2, and back and forth. Mrk 1018 had changed from a Type 1.9 to a Type 1 Seyfert, and changed back to Type 1.9 after 30 years (Cohen et al. 1986; McElroy et al. 2016). Observations over more than 40 years reveal that Mrk 590

changed from Type 1.5 to Type 1 and changed back to Type 1.9-2 (Denney et al. 2014). NGC 2617, which was a Seyfert 1.8 galaxy (Moran et al. 1996), changed to a Seyfert 1 (Shappee et al. 2014). These cases are better explained as changes in luminosity rather than obscuration (Denney et al. 2014; Shappee et al. 2014; McElroy et al. 2016). The broad emission lines of NGC 4151, which was originally Type 1.5 (Osterbrock 1977), had once disappeared (Antonucci & Cohen 1983; Lyutyj et al. 1984; Penston & Perez 1984) and then returned (e.g., Shapovalova et al. 2010). The variation in NGC 4151 is explained as probably being caused by an accelerating outflow originating very close to the black hole (BH; Shapovalova et al. 2010). Such back-and-forth type changes encourage exploration of what mechanisms generate these changes.

In recent years, discoveries of CL quasars have shown that such transitional phenomena happen at higher redshifts and can occur in more luminous and massive systems. Until now, there were fewer than 20 known CL quasars. LaMassa et al. (2015) reported the first CL quasar, J0159+0033, which changed from Type 1 to Type 1.9. They demonstrated that variable absorption does not explain the observed timescales and large-scale obscuration material is needed for this scenario. Merloni et al. (2015) argued that J0159+0033 could be a luminous flare produced by a TDE. Runnoe et al. (2016) reported a CL quasar, J1011+5442, “turning-off” within a rest-frame time of approximately 500 days. They argued that the transition timescale is inconsistent with an abrupt change in the reddening toward the central engine, and the decaying light curve with a prolonged bright state preceding the decay is not consistent with a decaying TDE. If the type changes were caused by the obscuration of the quasar, high linear polarization would be expected (Hutsemékers et al. 2017; Marin 2017). Hutsemékers et al. (2017) measured the polarization of J1011+5442, and found null polarization, suggesting that the type transition was not due to variable obscuration. A rapid “turn-on” of a quasar, J1554+3629, was detected by iPTF on a timescale of less than one year (Gezari et al. 2017). They implied that a factor of 10 brightening in UV and X-ray continuum flux is more likely caused by an intrinsic change in the accretion rate. Some systematic archival searches for objects in the Sloan Digital Sky Survey (SDSS) with repeat spectroscopy found more CL quasars (MacLeod et al. 2016; Ruan et al. 2016). They implied that changes in the accretion rate can better explain the transition timescale and emission-line properties than variable dust obscuration. Sheng et al. (2017) argued that the large variability amplitude of CL AGNs in the mid-infrared supports the scenario in which changes in the accretion rate occurs for reasons other than varying obscuration. In a recent TDE (PS16dtm), broad Balmer emission lines appeared to be accompanied by a significant increase in the continuum flux, as well as strong Fe II and He II emissions (Blanchard et al. 2017).

The frequency and timescale of such transients in the universe are interesting issues. Martini & Schneider (2003) suggested that the number of turn-off quasars in a large number of quasars can be used to measure or set a lower limit on the episodic lifetime of quasars. In the search by MacLeod et al. (2016), out of more than 1000 quasars with g -band variability larger than one mag, only 10 objects showed variable broad emission lines (MacLeod et al. 2016). The majority of highly variable quasars did not exhibit emerging or disappearing broad emission lines. Rumbaugh et al. (2018) identified ~ 1000

extreme variability quasars (EVQs) with a maximum g -band magnitude change of more than one mag with the SDSS and 3 Year Dark Energy Survey (DES, Flaugher 2005) imaging. They claimed that these EVQs are good candidates for CL AGNs.

CL AGNs provide perfect cases to study the connection between AGNs and their host galaxies. There is a tight correlation between BH mass, M_{BH} , and the velocity dispersion, σ_* , of the bulge component in nearby galaxies (Kormendy & Ho 2013). Gezari et al. (2017) reported that the M_{BH} ($2_{-1.5}^{+4} \times 10^8 M_\odot$) of J1554+3629 ($z = 0.237$), estimated from the quasar spectrum after “turning on” with emerging broad Balmer emission lines, is in good agreement with its M_{BH} ($1_{-0.7}^{+2} \times 10^8 M_\odot$) inferred from σ_* . CL AGNs provide exceptional opportunities to provide the central BHs and their host galaxies at higher redshift. On the other hand, the “turning-off” CL quasars provide perfect opportunities to study the host galaxies of quasars in detail, avoiding contamination from the luminous central engines.

The CL AGNs, with the appearance or disappearance of broad Balmer lines on a timescale of years, challenge our understanding of the AGN unification model. Motivated by an interest in determining the physical mechanism behind type transitions, and questions regarding the frequency and timescale of the type transition, we conduct a survey for CL AGNs. The investigations consist of (1) repeat spectroscopy in the SDSS spectral archive, (2) repeat spectroscopy in the SDSS and the Large Sky Area Multi-Object Fiber Spectroscopic Telescope (LAMOST) spectral archive, and (3) searching for CL candidates based on photometric variability.

This paper is organized as follows. Section 2 describes the spectroscopic and imaging data. Section 3 outlines the selection methods and spectroscopic observations. In Section 4, we present new CL AGNs and their variability in the optical and mid-infrared. In Section 5, we discuss the CL AGN color variability and the timescale of the type transition. We summarize the paper in Section 6. In this work we adopt a standard Λ CDM cosmology with $\Omega_\Lambda = 0.7$, $\Omega_m = 0.3$, and $H_0 = 70 \text{ km s}^{-1} \text{ Mpc}^{-1}$. Throughout this paper, all magnitudes are in AB magnitudes.

2. Data

2.1. Spectroscopic Data

2.1.1. SDSS Spectroscopy

There are 4,851,200 spectra in the SDSS Fourteenth Data Release (DR14; Abolfathi et al. 2017) taken by the Sloan Foundation 2.5 m telescope (Gunn et al. 2006) at Apache Point Observatory. The spectra are from the SDSS-I/II, with a wavelength coverage from 3800 to 9100 Å, and the Baryon Oscillation Spectroscopic Survey (BOSS; Dawson et al. 2013) spectrograph of the SDSS-III (Eisenstein et al. 2011), with a wavelength coverage from 3600 to 10400 Å (Smee et al. 2013). The spectral resolution is 1500 at 3800 Å and 2500 at 9000 Å. The SDSS spectroscopic pipelines classify the objects as galaxies (“GALAXY”), stars (“STAR”), or quasars (“QSO”), through a comparison of individual spectra with galaxy, QSO, and stellar templates (Bolton et al. 2012; Hutchinson et al. 2016). The spectral quality is described by a confidence flag titled “zWarning,” which is 0 or 16 for good data without identified problems (e.g., Stoughton et al. 2002). We carry out searches of CL AGNs from SDSS galaxies or quasars.

2.1.2. LAMOST Spectroscopy

LAMOST is a 4 m reflecting Schmidt telescope equipped with 4000 fibers with a 5° field of view (Cui et al. 2012; Zhao et al. 2012). The wavelength coverage of LAMOST ranges from 3700 Å to 9000 Å, with two arms (Du et al. 2016), a blue arm (3700–5900 Å) and a red arm (5700–9000 Å). The overall spectral resolution of LAMOST is approximately 1800. The data are reduced with LAMOST pipelines (Luo et al. 2012). In this paper, we utilize the LAMOST spectra from data releases one to five (Luo et al. 2015; He et al. 2016).

2.2. Imaging Data

CL AGNs showed continuum flux changes in the optical and mid-infrared. Apart from objects with repeat spectroscopy, we carry out additional searches of CL AGNs based on imaging data. We briefly introduce the imaging data as follows.

The SDSS imaging survey scanned the sky in five filters, *ugriz* (Fukugita et al. 1996), covering 11,663 deg² in SDSS-I/II from 2000 to 2007 (Abazajian et al. 2009) and an additional 3,000 deg² in SDSS-III in 2008.

The Pan-STARRS1 (PS1; Chambers et al. 2016) survey used a 1.8-meter telescope with a 1.4 Gigapixel camera to image the sky in five broadband filters (*grizy*). The observations cover three-quarters of the sky several times per filter. We use the PS1 magnitudes in the stack catalog, from co-added images made from the multiple exposures. Using a quasar composite spectrum from Vanden Berk et al. (2001) convolved with the PS1 and SDSS *g*-band filter curves (Equation (2) in Wu et al. 2004), the magnitude difference, $\delta(g_{\text{PS1}} - g_{\text{SDSS}})$, is between -0.065 mag and 0.008 mag at redshift $z < 2$.

The DESI Legacy imaging survey (DELS; Dey et al. 2018) commenced imaging surveys, including the DECam Legacy Survey (DECaLS) *g*-, *r*-, and *z*-bands, the *g*- and *r*-bands of the Beijing–Arizona Sky Survey (BASS; Zou et al. 2017), and the Mayall *z*-band Legacy Survey (MzLS). The imaging survey commenced from 2014 and will conclude in 2018, covering 14000 deg² sky. The magnitude difference, $\delta(g_{\text{DELS}} - g_{\text{SDSS}})$, is between -0.053 mag and 0.005 mag at $z < 2$, using the composite spectrum convolved with the DELS and SDSS *g*-band filter curves.

The *Wide-field Infrared Survey Explorer* (WISE; Wright et al. 2010) mapped the all-sky from 2010 January to July in four bands centered at wavelengths of 3.4, 4.6, 12, and 22 μm (*W1*, *W2*, *W3*, and *W4*). The secondary cryogen survey and Near-Earth Object Wide-field Infrared Survey Explorer (NEOWISE; Mainzer et al. 2011) Post-Cryogenic Mission mapped the sky from 2010 August to 2011 February. The NEOWISE Reactivation Mission (NEOWISE-R; Mainzer et al. 2014) surveys the sky in the *W1* and *W2* bands from 2013. We use WISE multi-epoch photometry from individual single-exposure images in the *W1* and *W2* bands.

The Catalina Real-time Transient Survey (CRTS; Drake et al. 2009) uses data from the Catalina Sky Survey, which repeatedly covers 26,000 deg² on the sky. The CRTS photometric data are unfiltered and calibrated to *V*-band magnitude. We apply a constant offset to the CRTS magnitudes to match the simultaneous *g*-band PS1 magnitude.

The Palomar Transient Factory (PTF; Law et al. 2009) is a wide-field survey covering approximately 30,000 deg² in the *g*- and *r*-bands from 2009 to 2012.

3. Target Selection and Observation

3.1. SDSS Repeat Spectroscopy

We carried out a systematic investigation in the SDSS DR14 spectral archive, in which 87% of spectra are good quality ($z\text{Warning} = 0$ or 16). Cross-matching the spectra with a radius of $2''$ results in 350,609 objects repeatedly observed (≥ 2 epochs). There were 175,575 repeatedly observed objects classified as “GALAXY” by the SDSS pipeline in at least one epoch spectrum. Among them, 2,023 objects were classified as “GALAXY” in one epoch of the spectrum and “QSO” in another epoch of the spectrum. We visually checked all the spectra of these objects to search for CL AGNs.

Because the definitions of AGN spectral types depend on the strength of broad emission lines, we qualitatively define a detection of a broad emission line if the signal-to-noise ratio (S/N) of the emission line is higher than 5 or as a non-detection if the S/N is lower than 1. Specifically, a weak detection is when the S/N is between 1 and 3, and an intermediate detection is when the S/N is between 3 and 5. Visual checks cannot accurately discern the quantitative changes of emission lines, but they can qualitatively distinguish the cases with dramatic changes. More specifically, with a visual inspection it is easier to distinguish $>5\sigma$ and $<1\sigma$ detections than to distinguish 3σ – 5σ and 1σ – 3σ detections. Therefore, the visual inspection process is inclined to select AGNs that changed between Type 1 and Type 2 (or Type 1.9), with an appearing or disappearing broad H α (or H β) emission line. Nevertheless, a visual check selects AGNs that changed between Type 1 and Type 1.8 with a lower completeness. Objects with distinct companions (within $2''$) in the SDSS image were also excluded in the visual check process. From the visual inspection, we selected 9 CL AGNs. Four of the selected CL AGNs were reported previously, including the CL quasar J0159+0033 in LaMassa et al. (2015), J0126–0839 and J2336+0017 in Ruan et al. (2016), and J1011+5442 in Runnøe et al. (2016). We recovered all the changing-look quasars in these three works. The new CL AGNs found in the SDSS archive are J1104+6343, J1118+3203, J1150+3632, J1358+4934, and J1533+0110. We describe the objects rejected by visual inspection in the Appendix. In Section 4.1, we describe the fitting of the H α and H β lines of these objects to quantitatively understand the changes of CL AGNs selected from visual inspection. The ratio of CL AGNs with an appearance or disappearance of broad Balmer emission lines is roughly 0.006%, for objects that were identified as galaxies and repeatedly observed. This ratio may be affected by some issues, for example, the time intervals of the repeat spectra, spectroscopic survey selection bias, spectral quality, and possible selection bias of visual inspection. The selection steps are summarized in Table 1.

3.2. LAMOST and SDSS Repeat Spectroscopy

We cross-matched the LAMOST spectral archive with the SDSS spectra archive. The selection steps are summarized in Table 2. There were 155,220 objects that were classified as “GALAXY” (75%) or “QSO” (25%) with good spectral quality in the SDSS, or were observed in LAMOST. Comparing the SDSS spectra with the LAMOST spectra, we fit the Balmer emission lines in spectra from the SDSS and the LAMOST with Gaussian profiles. We selected the objects with changes in the emission-line flux density larger than $2 \times 10^{-18} \text{ erg s}^{-1} \text{ cm}^{-2} \text{ \AA}^{-1}$, which is a conservative criterion

Table 1
CL AGNs Selection from SDSS Repeat Spectra

Note	Selection	Number
Spectra in SDSS DR14	All	4,851,200 spectra
Spectra with good quality	$z_{\text{Warning}} = 0$ or 16	4,196,290 spectra
Objects with repeat spectra	2'' coordinates cross-match	350,609 objects
Galaxies with repeat spectra	classified as "GALAXY" at one epoch	175,575 objects
Classification changed between QSO and Galaxy	classified as "QSO" at another epoch	2,023 objects
Visual check	appearing or disappearing broad $H\beta$	9 (4 known) CL AGNs

Table 2
CL AGNs Selection from SDSS and LAMOST Repeat Spectra

Note	Selection	Number
Spectra with good quality	$z_{\text{Warning}} = 0$ or 16	4,196,290 spectra
SDSS QSO/Galaxy	classified as "GALAXY" or "QSO"	3,223,478 spectra
Repeatedly observed by LAMOST	2'' cross-match with LAMOST	155,220 objects
Possible variable Balmer lines	program to automatically check emission-line variation	8,181 objects
Visual check	appearing or disappearing broad $H\beta$	10 CL AGNs

avoiding missing CL AGNs at this step. There were 8,181 objects with potential emission-line variation. We visually inspected all these objects, and identified 10 CL AGNs, including 8 turn-on CL AGNs (J0831+3646, J0909+4747, J0937+2602, J1115+0544, J1132+0357, J1447+2833, J1545+2511, and J1552+2737) and 2 turn-off AGNs (J0849+2747 and J1152+3209). We obtained flux calibrations to match the narrow emission-line flux of the SDSS spectra, assuming a constant narrow emission-line flux within a few tens of years. We describe the objects visually rejected in the [Appendix](#). In this survey, about 0.007% of the galaxies from the LAMOST and SDSS cross-matched sample were proven to be CL AGNs with the appearance of broad Balmer emission lines.

3.3. Photometric Variability

Most of the reported CL AGNs were discovered by repeat spectroscopy. Meanwhile, the optical and mid-infrared flux of CL AGNs varies following the type transition. We conducted additional CL AGN searches based on photometric variability. We searched CL AGN candidates from objects that were spectroscopically identified as "GALAXY" but brightened in later photometric data, and from objects that were spectroscopically identified as "QSO" but significantly dimmed.

3.3.1. Turn-on CL AGNs Selected from Imaging Data

We carried out a search for turn-on CL AGNs from SDSS galaxies, which became brighter later. The selection procedures are shown in Table 3. Motivated by the rapid transition that happened in J1011+5442 and J1554+3629, we first considered recent imaging data. The *WISE* multi-epoch data are available for recent years, from 2010 to 2017. We started from galaxies detected by *WISE* multi-epoch data, and there were 28,395 galaxies that became brighter ($\Delta W1 < -0.2$ mag) and redder ($\Delta(W1 - W2) > 0.1$ mag) in the mid-infrared. A more detailed discussion about the color criteria in the mid-infrared will be provided in Section 5.1. Among them, 2147 galaxies also became brighter in the optical *g*-band and had $g < 19$ mag. We checked the CRTS and PTF light curves of these galaxies at $z > 0.1$, and picked out 59 turn-on CL AGN candidates with a clear trend of increasing flux in the optical

and mid-infrared. This selection method recovered J0831+3646 and J1554+3629. Other turn-on CL AGNs from repeat spectroscopy were missed in this process due to smaller redshift or smaller variability. More systematic searches can be extended to lower redshifts and fainter objects with less variability.

Optical long-slit spectroscopic observations for some CL AGN candidates were carried out using the Xinglong 2.16 m telescope (XLT) in China and Palomar P200/DBSP spectrograph. The Xinglong 2.16 m telescope is located at the NAOC observatory. It is equipped with the Beijing Faint Object Spectrograph and Camera (BFOSC). We observed 17 CL AGN candidates in 2017 April, including a CL AGN J1554+3629 discovered by Gezari et al. (2017), using the BFOSC and Grism 4 (G4) with a dispersion of 198 Å/mm and a wavelength coverage from 3850 to 8300 Å. The grism yields a resolution of $R \sim 265$ or 340 at 5000 Å using a 2''/3 or 1''/8 slit (Fan et al. 2016). The spectra were obtained using a 1''/8 slit when seeing $< 2''$ or a 2''/3 slit when $2'' < \text{seeing} < 3''$. J1259+5515 was observed by DBSP after it was observed by XLT. The DBSP spectrum was obtained using P200/DBSP with grating G600 at the blue side ($R \sim 1200$ at 5000 Å) and G316 at the red side ($R \sim 642$ at 5000 Å) with a 1''/5 slit under seeing $\sim 1''/5$. The spectra were reduced using standard IRAF⁴ routines (Tody 1986, 1993). The flux of J1259+5515 obtained with DBSP and XLT in two days are in good agreement. Five new CL AGNs (J1003+3525, J1110-0003, J1259+5515, J1319+6753, and J1550+4139), with emerging broad $H\beta$, were confirmed by the XLT and DBSP spectra. The fiber diameters of SDSS, BOSS, and LAMOST are 3'', 2'', and 3''/3, respectively. The fiber diameters are large enough to include the light from the nuclear. The slit widths of long-slit spectra are slightly smaller than the fiber diameters, leading to less host galaxy light contributions to the spectra. The photometric variability of these CL AGNs rules out the possibility that the different spectra are merely caused by differences between fiber and slit spectra.

⁴ IRAF is distributed by the National Optical Astronomy Observatory, which is operated by the Association of Universities for Research in Astronomy (AURA) under cooperative agreement with the National Science Foundation.

Table 3
Turn-on CL AGN Candidate Selection Based on Imaging Data

Note	Selection	Number
Spectra in SDSS DR14	all	4,851,200 spectra
WISE single-epoch detected	2'' cross-match with the WISE single-epoch data	4,196,290 spectra
Galaxies with good spectra	class="GALAXY" and $z_{\text{Warning}} = 0$ or 16)	2,494,319 spectra
WISE brighten and redder	$\Delta W1 < -0.2$ and $\Delta(W1 - W2) > 0.1$	28,395 objects
Optical brighten	$\Delta g < 0$ and $g < 19$	2147 objects
Redshift	$z > 0.1$	660 objects
Visual check light curves	obvious brighten trend (CRTS/PTF)	59 objects
Observed	...	17 objects
Confirmed	...	6 (1 known) CL AGNs

Table 4
Turn-off CL AGN Candidate Selection Based on Imaging Data

Note	Selection	Number
SDSS QSO in DR7 and DR12	All	346,464 objects
WISE single-epoch detected	2'' cross-match with the WISE single-epoch photometry	326,124 objects
WISE dim and bluer	$\Delta W1 > 0.2$ and $\Delta(W1 - W2) < -0.1$	6,847 objects
Optical dim	$\Delta g > 1$	232 objects
Observed	...	1 objects
Confirmed	...	1 CL AGN c

3.4. Turn-off CL AGNs Selected from Imaging Data

We conducted a survey of turn-off CL AGNs from SDSS quasar catalogs (shown in Table 4). There are 346,464 quasars (Yang et al. 2017) in the SDSS Data Release 7 Quasar catalog (Schneider et al. 2010) and the Data Release 12 Quasar catalog (P  ris et al. 2017). Cross-matching with a radius of 2'', 94% of quasars were detected in the WISE multi-epoch data. There were 6,847 quasars that dimmed ($\Delta W1 > 0.2$ mag) and became bluer ($\Delta(W1 - W2) < -0.1$ mag) in the mid-infrared.

On a timescale of months to years, the continuum variability of quasars is typically 0.2 mag in the optical (e.g., Vanden Berk et al. 2004; Wilhite et al. 2005; MacLeod et al. 2012). Among the quasars with mid-infrared variability, 232 quasars also dimmed significantly in the optical (more than 1 mag in the g -band). We recovered two turn-off CL AGNs, including J0849+2747 and J1011+5442. In 2017 April, we observed one candidate (with the XLT using a 2''3 slit), J1104+0118, with g -band and $W1$ -band magnitudes dimmed by more than 1.8 mag and 0.6 mag, respectively. The continuum flux of J1104+0118 obviously became much redder than that in the SDSS spectrum, and the broad Mg II emission line was not detected in the new spectrum. Higher-quality spectra are needed for a more detailed analysis. A more complete survey of CL AGNs will require more spectroscopic follow-up.

4. Results

4.1. New CL AGNs

In total, there are 21 new CL AGNs found in our surveys (summarized in Table 5). Among the new CL AGNs, 5 were found by repeat spectra from the SDSS, 10 were discovered based on repeat spectra from SDSS and LAMOST, and 6 were selected from photometric variability in optical and mid-infrared imaging data, and confirmed by new spectroscopy.

The five known CL AGNs that we recovered are also listed in Table 5. Figure 1 shows an example of the light curves (left panels), and spectra (right panels) of a new CL AGN, J0831+3646. The light curves and spectra of the other 20 new CL AGNs are listed in the Appendix. In Figure 1, the spectra separating for 13 years show that there was no $H\beta$ emission in 2002 in the SDSS (black), while the broad $H\beta$, as well as broad $H\alpha$, emission lines emerged in the spectra taken in 2015 in LAMOST (blue). The residual spectrum (gray spectrum at the bottom of the right panel), between the bright epoch and faint epoch spectra, distinctly shows the emerging of broad $H\beta$ and $H\alpha$. The left panel in Figure 1 shows the photometric data from several surveys, including SDSS, PS1, DELS, WISE, CRTS, and PTF. The imaging data taken in separated epochs help identify the variability of objects.

We fit the spectra of all the CL AGNs with a quasar spectral fitting procedure (QSfit, Calderone et al. 2017), considering the contribution from the AGN continuum, Balmer continuum, host galaxy, blended iron lines, broad emission lines, and narrow emission lines. The spectroscopic measurements are summarized in Table 6. The later epoch spectrum is calibrated to the earlier SDSS spectrum assuming a constant narrow emission line during a few years. Only in 4 out of these 21 objects is the S/N of the faint-state spectrum lower than that of the bright state spectrum. The weaker Balmer emission-line intensity at the faint state is not a result of a worse observational condition.

According to the definition of AGN spectral types, we mark the spectral type as Type 1 when there are ($>5\sigma$) broad $H\beta$ components detected and Type 2 when the S/N of the broad $H\alpha$ is lower than 5. Specifically, when ($>5\sigma$) $H\alpha$ is detected, we mark the spectral type as Type 1.9 (1.8 or 1.5) when there is no, $<1\sigma$, (weak, 1σ – 3σ , or intermediate, 3σ – 5σ) broad $H\beta$ detected. As the Balmer emission lines disappeared in some spectra, we freed the parameter limit of the amplitude of the line fitting, which was assumed to be positive. The fitting results are shown in Table 6. The negative luminosity means that there is absorption instead of emission lines. As shown in Table 6, six CL AGNs transitioned between Type 1 and Type 2 classes, and 10 CL AGNs transitioned between Type 1 and Type 1.9 classes. In addition, the fitting procedure recognizes $>5\sigma$ broad $H\beta$ emission lines in both bright and faint-state spectra of J1118+3203 and J1152+3209, and $<1\sigma$ broad $H\beta$ lines in both bright and faint-state spectra of J1552+2737. Therefore, these three AGNs fail to fit the quantitative definition above. While the dramatic $H\beta$ luminosity changes show that $H\beta$ faded in J1118+3203 and J1152+3209 (marked as "off*" in Table 6) and enhanced in J1152+3209 (marked as "on*" in Table 6). Among them, 15 AGNs turned on, with

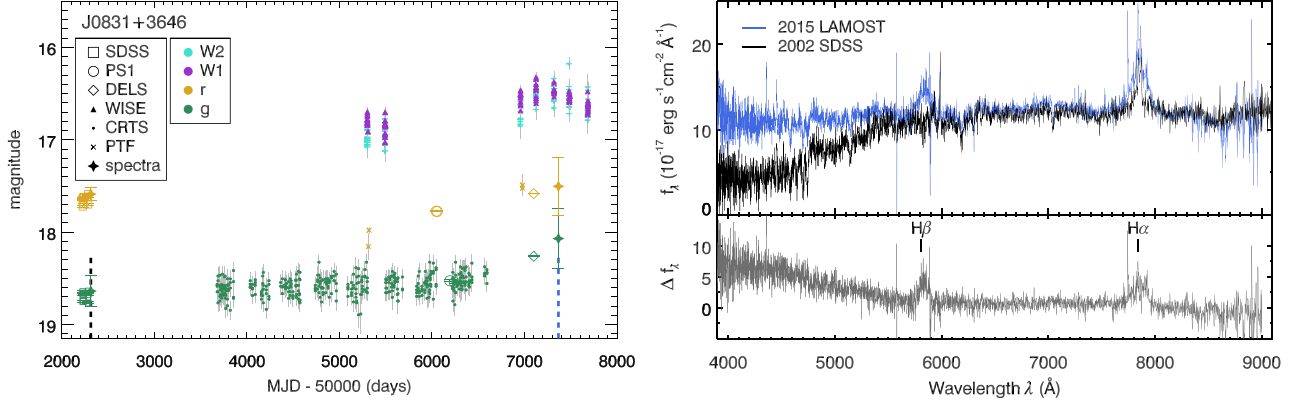


Figure 1. Example of the light curves (left panel) and spectra (right panel) of a new CL AGN, J0831+3646. In the left panel, all photometric data are expressed in magnitude, and the x-axis is MJD–50000. Photometric data in distinct bands are shown in different colors, including the g (green), r (yellow), W1 (magenta), and W2 (cyan) band photometry. The different shapes represent data from different surveys, including SDSS (open square), PS1 (open circle), DELS (open diamond), WISE W1 (solid triangle), WISE W2 (cross), CRTS (solid dots), and PTF (x shape). The vertical dashed lines show the epochs of the spectra. The right panel shows the spectral flux density, f_λ , of CL AGNs in units of $10^{-17} \text{ erg s}^{-1} \text{ cm}^{-2} \text{ \AA}^{-1}$. The early-epoch SDSS spectrum is plotted in black, and the new epoch spectrum is colored blue if the AGN turned on, or red if the AGN turned off. The lower panel shows the spectra difference, Δf_λ , between the bright epoch and faint epoch spectra. The vertical bars mark the locations of appeared or disappeared broad emission lines. The light curves and spectra of the other 20 CL AGNs are in the [Appendix](#).

Table 5
CL AGNs

Name	R.A.	Decl.	Redshift	Transition	Epoch	Instrument2	References
J0831+3646	08:31:32.25	+36:46:17.2	0.19501	Turn-on	[52312, 57367]	LAMOST	This work
J0849+2747	08:49:57.78	+27:47:28.9	0.29854	Turn-off	[53350, 56628]	LAMOST	This work
J0909+4747	09:09:32.02	+47:47:30.6	0.11694	Turn-on	[52620, 57745]	LAMOST	This work
J0937+2602	09:37:30.32	+26:02:32.1	0.16219	Turn-on	[54524, 57369]	LAMOST	This work
J1003+3525	10:03:23.47	+35:25:03.8	0.11886	Turn-on	[53389, 57867]	XLT	This work
J1104+0118	11:04:55.17	+01:18:56.6	0.57514	Turn-off	[52374, 57867]	XLT	This work
J1104+6343	11:04:23.21	+63:43:05.3	0.16427	Turn-off	[52370, 54498]	SDSS	This work
J1110–0003	11:10:25.44	–00:03:34.0	0.21922	Turn-on	[51984, 57864]	XLT	This work
J1115+0544	11:15:36.57	+05:44:49.7	0.08995	Turn-on	[52326, 57393]	LAMOST	This work
J1118+3203	11:18:29.64	+32:03:59.9	0.3651	Turn-off	[53431, 56367]	BOSS	This work
J1132+0357	11:32:29.14	+03:57:29.0	0.09089	Turn-on	[52642, 57392]	LAMOST	This work
J1150+3632	11:50:39.32	+36:32:58.4	0.34004	Turn-off	[53436, 57422]	BOSS	This work
J1152+3209	11:52:27.48	+32:09:59.4	0.37432	Turn-off	[53446, 57844]	LAMOST	This work
J1259+5515	12:59:16.74	+55:15:07.2	0.19865	Turn-on	[52707, 57863]	XLT/DBSP	This work
J1319+6753	13:19:30.75	+67:53:55.4	0.16643	Turn-on	[51988, 57867]	XLT	This work
J1358+4934	13:58:55.82	+49:34:14.1	0.11592	Turn-on	[53438, 54553]	SDSS	This work
J1447+2833	14:47:54.23	+28:33:24.1	0.16344	Turn-on	[53764, 57071]	LAMOST	This work
J1533+0110	15:33:55.99	+01:10:29.7	0.14268	Turn-on	[51989, 54561]	SDSS	This work
J1545+2511	15:45:29.64	+25:11:27.9	0.11696	Turn-on	[53846, 57891]	LAMOST	This work
J1550+4139	15:50:17.24	+41:39:02.2	0.22014	Turn-on	[52468, 57864]	XLT	This work
J1552+2737	15:52:58.30	+27:37:28.4	0.08648	Turn-on	[53498, 56722]	LAMOST	This work
J0126–0839	01:26:48.08	–08:39:48.0	0.19791	Turn-off	[52163, 54465]	SDSS	Ruan et al. (2016)
J0159+0033	01:59:57.64	+00:33:10.5	0.31204	Turn-off	[51871, 55201]	BOSS	LaMassa et al. (2015)
J1011+5442	10:11:52.98	+54:42:06.4	0.24639	Turn-off	[52652, 57073]	BOSS	Runnoe et al. (2016)
J1554+3629	15:54:40.26	+36:29:51.9	0.23683	Turn-on	[53172, 57862]	XLT	Gezari et al. (2017)
J2336+0017	23:36:02.98	+00:17:28.7	0.24283	Turn-off	[52199, 55449]	BOSS	Ruan et al. (2016)

Note. “Epoch” shows the MJD of the two epoch spectra. “Instrument2” indicates the spectrograph or telescope of the recent spectrum. XLT represents the Xinglong 2.16 m telescope at NAOC.

broad Balmer emission lines emerging (or enhancing), as well as increased broadband flux. The broad Balmer lines of 6 CL AGNs disappeared (or faded), accompanied by dimming in the continuum. Among the 21 CL AGNs, 17 CL AGNs showed broad $H\alpha$, $H\beta$, $H\gamma$, or even $H\delta$ appeared or disappeared. Only broad $H\alpha$ and $H\beta$ changes were detected in J0831+3646, J1319+6753, and J1552+2737; clear emerging of broad $H\alpha$ and $H\beta$ emission lines, and increased flux in the optical and mid-infrared, confirmed their changes.

4.2. CL AGN Optical and Mid-infrared Variability

The continuum flux varies along with the CL AGN type transition. Table 7 summarizes the photometric variability of CL AGNs. We obtain the g -band variability, Δg , from the magnitude offset between the PS1 g -band magnitude, or the DELS g -band magnitude when available, and the SDSS g -band magnitude. We use the first epoch SDSS photometry if there are data at more than one epoch. The uncertainties of Δg are

Table 6
Spectral Type Transition of CL AGNs

Name	Redshift	λL_{5100} (10^{42} erg s $^{-1}$)	S/N ₁	S/N ₂	$L_{H\beta,1}$ (10^{41} erg s $^{-1}$)	$L_{H\beta,2}$ (10^{41} erg s $^{-1}$)	$L_{H\alpha,1}$ (10^{41} erg s $^{-1}$)	$L_{H\alpha,2}$ (10^{41} erg s $^{-1}$)	S/N _{Hβ1}	S/N _{Hβ2}	S/N _{Hα1}	S/N _{Hα2}	E1	E2	Type
J0831+3646	0.19501	18.23 \pm 0.24	12.3	10.9	-4.05 \pm 0.33	2.85 \pm 0.39	3.60 \pm 1.00	10.19 \pm 0.42	-12.1	7.3	3.6	24.2	2	1	on
J0849+2747	0.29854	63.42 \pm 1.48	9.3	2.7	8.56 \pm 0.39	-2.81 \pm 2.03	22.76 \pm 1.95	2.49 \pm 0.97	22.2	-1.4	11.7	2.6	1	2	off
J0909+4747	0.11694	6.97 \pm 0.20	11.0	8.5	-1.88 \pm 0.13	1.32 \pm 0.18	1.48 \pm 0.13	7.39 \pm 0.13	-14.9	7.5	11.8	57.1	1.9	1	on
J0937+2602	0.16219	6.85 \pm 0.32	20.9	7.1	-1.71 \pm 0.13	1.75 \pm 0.20	3.66 \pm 0.24	11.93 \pm 2.04	-12.8	8.6	15.4	5.9	1.9	1	on
J1003+3525	0.11886	45.77 \pm 1.64	15.6	6.9	-1.40 \pm 0.12	10.30 \pm 1.02	2.34 \pm 0.57	12.58 \pm 0.63	-11.7	10.1	4.1	19.9	2	1	on
J1104+0118	0.57514	302.41 \pm 6.30	7.0	0.7	79.89 \pm 5.19	-43.38 \pm 13.61	15.4	-3.2	1	2	off
J1104+6343	0.16427	4.46 \pm 0.49	6.0	6.1	1.14 \pm 0.14	0.33 \pm 0.11	4.90 \pm 0.16	0.79 \pm 0.13	7.9	3.0	31.6	6.2	1	1.8	off
J1110-0003	0.21922	48.61 \pm 1.34	8.0	6.1	0.27 \pm 0.10	6.70 \pm 0.92	1.78 \pm 0.71	11.98 \pm 1.01	2.8	7.3	2.5	11.9	2	1	on
J1115+0544	0.08995	17.27 \pm 0.27	18.9	8.7	-1.23 \pm 0.07	2.46 \pm 0.18	0.05 \pm 0.07	7.92 \pm 1.11	-18.4	14.0	0.7	7.2	2	1	on
J1118+3203	0.3651	56.48 \pm 2.29	4.9	4.9	11.76 \pm 1.11	2.90 \pm 0.51	...	10.31 \pm 0.57	10.6	5.7	...	18.0	1	1	off*
J1132+0357	0.09089	16.26 \pm 0.38	17.3	7.4	-3.23 \pm 0.08	4.74 \pm 0.40	0.78 \pm 0.05	2.40 \pm 0.17	-40.2	11.8	15.9	14.1	1.9	1	on
J1150+3632	0.34004	39.01 \pm 2.28	4.9	5.2	5.02 \pm 0.53	-3.29 \pm 0.49	22.24 \pm 1.25	3.18 \pm 0.40	9.4	-6.7	17.8	7.9	1	1.9	off
J1152+3209	0.37432	138.05 \pm 2.68	11.9	3.7	38.31 \pm 1.16	10.53 \pm 1.29	33.0	8.2	1	1	off*
J1259+5515	0.19865	17.95 \pm 0.91	7.4	3.5	0.02 \pm 0.24	5.53 \pm 0.82	4.30 \pm 0.38	9.21 \pm 3.88	0.1	6.8	11.4	2.4	1.9	1	on
J1319+6753	0.16643	30.90 \pm 1.46	12.1	7.3	0.36 \pm 0.33	7.96 \pm 1.16	2.37 \pm 0.27	5.90 \pm 4.43	1.1	6.8	8.6	1.3	1.9	1	on
J1358+4934	0.11592	5.50 \pm 0.19	7.8	13.1	0.36 \pm 0.09	0.96 \pm 0.10	0.74 \pm 0.06	1.98 \pm 0.10	3.8	9.2	13.4	19.0	1.9	1	on
J1447+2833	0.16344	66.68 \pm 0.97	7.8	13.1	-1.16 \pm 0.29	2.49 \pm 0.24	2.27 \pm 0.19	11.63 \pm 0.25	-3.9	10.6	12.2	47.2	1.9	1	on
J1533+0110	0.14268	<1.00	14.2	13.4	-3.98 \pm 0.17	0.54 \pm 0.12	1.00 \pm 0.15	3.97 \pm 0.29	-23.6	4.4	6.9	13.7	1.9	1.5	on
J1545+2511	0.11696	6.81 \pm 0.06	19.6	17.1	-2.16 \pm 0.15	0.71 \pm 0.11	1.69 \pm 0.12	5.90 \pm 0.14	-14.4	6.7	14.4	41.3	1.9	1	on
J1550+4139	0.22014	28.26 \pm 1.30	11.6	8.1	-4.41 \pm 0.47	15.71 \pm 1.48	2.47 \pm 0.40	14.01 \pm 0.89	-9.5	10.6	6.2	15.8	1.9	1	on
J1552+2737	0.08648	<1.00	12.3	7.8	-3.67 \pm 0.05	-1.34 \pm 0.10	0.38 \pm 0.04	2.70 \pm 0.05	-69.2	-13.9	9.8	59.1	1.9	1.9	on*

Note. λL_{5100} is the continuum luminosity at 5100 Å in the bright epoch spectrum. J1533+0110 and J1552+2737 are too red to fit a power-law continuum, with an upper limit of 1.00×10^{42} erg s $^{-1}$. S/N₁ and S/N₂ are the median S/N pixel $^{-1}$ of the former and recent epoch spectra, respectively. $L_{H\beta,1}$, ($L_{H\alpha,1}$) and $L_{H\beta,2}$ ($L_{H\alpha,2}$) are the luminosities of the broad H β (H α) component in the former and recent epoch spectra. The negative luminosity means that there is absorption instead of emission lines. There is no H α data when H α moves out of the range of the spectrum. S/N_{H β 1} (S/N_{H α 1}) and S/N_{H β 2} (S/N_{H α 2}) are the S/Ns of broad H β (H α) components in the former and recent epoch spectra. E1 and E2 describe the spectral types of the former and recent epoch spectra. Type describes the transition type.

Table 7
Variability of Changing-look AGNs

Name	Survey	Δg_{phot} (mag)	$\Delta(g-r)_{\text{phot}}$ (mag)	Δg_{spec} (mag)	$\Delta(g-r)_{\text{spec}}$ (mag)	$\Delta W1$ (mag)	$\Delta(W1-W2)$ (mag)	δ_{CRTS} (mag)
J0831+3646	DELS	-0.41 ± 0.01	-0.35 ± 0.02	-0.57 ± 0.37	-0.48 ± 0.49	-0.35 ± 0.10	0.13 ± 0.14	1.15
J0849+2747	DELS	0.31 ± 0.01	0.29 ± 0.02	1.00 ± 0.65	0.69 ± 0.80	0.28 ± 0.13	-0.24 ± 0.21	1.17
J0909+4747	PS1	0.06 ± 0.01	-0.03 ± 0.02	-0.71 ± 0.29	-0.39 ± 0.39	-0.42 ± 0.10	0.10 ± 0.18	0.90
J0937+2602	DELS	-0.17 ± 0.01	-0.06 ± 0.01	-0.29 ± 0.32	-0.24 ± 0.44	-0.41 ± 0.10	0.07 ± 0.15	0.92
J1003+3525	DELS	-0.52 ± 0.01	-0.27 ± 0.01	-1.17 ± 0.21	-0.54 ± 0.29	-0.58 ± 0.16	0.16 ± 0.26	0.92
J1104+0118	DELS	1.89 ± 0.03	1.48 ± 0.04	6.14 ± 111.71	4.98 ± 111.72	0.68 ± 0.11	-0.56 ± 0.26	1.68
J1104+6343	PS1	0.55 ± 0.02	0.44 ± 0.03	0.08 ± 0.46	0.11 ± 0.53	0.31 ± 0.24	0.03 ± 0.36	0.93
J1110-0003	DELS	-0.42 ± 0.02	-0.33 ± 0.02	-0.87 ± 0.40	-0.43 ± 0.53	-0.65 ± 0.12	0.11 ± 0.27	0.95
J1115+0544	DELS	-0.21 ± 0.01	-0.11 ± 0.01	-0.82 ± 0.22	-0.44 ± 0.30	-1.01 ± 0.10	0.59 ± 0.16	0.97
J1118+3203	PS1	0.67 ± 0.04	0.49 ± 0.05	0.80 ± 0.33	0.30 ± 0.43	0.15 ± 0.41	0.20 ± 0.58	1.50
J1132+0357	PS1	-0.11 ± 0.01	-0.15 ± 0.01	-1.16 ± 0.19	-0.55 ± 0.26	-0.56 ± 0.05	0.19 ± 0.12	0.91
J1150+3632	DELS	1.59 ± 0.02	0.92 ± 0.03	0.95 ± 0.41	0.50 ± 0.47	0.30 ± 0.24	0.18 ± 0.37	1.38
J1152+3209	PS1	1.36 ± 0.03	0.99 ± 0.03	1.39 ± 0.60	0.84 ± 0.76	0.19 ± 0.08	-0.27 ± 0.13	...
J1259+5515	DELS	-0.06 ± 0.02	-0.05 ± 0.02	-0.77 ± 0.93	-0.40 ± 0.99	-0.54 ± 0.10	0.26 ± 0.26	1.06
J1319+6753	PS1	-0.28 ± 0.01	-0.26 ± 0.01	-0.46 ± 0.40	-0.17 ± 0.47	-0.23 ± 0.07	0.10 ± 0.12	0.70
J1358+4934	DELS	0.41 ± 0.01	0.20 ± 0.02	-0.46 ± 0.20	-0.15 ± 0.24	0.00 ± 0.16	0.00 ± 0.23	0.80
J1447+2833	PS1	-0.15 ± 0.01	-0.18 ± 0.01	-0.72 ± 0.20	-0.46 ± 0.29	-0.45 ± 0.05	0.06 ± 0.08	0.85
J1533+0110	DELS	-0.14 ± 0.01	-0.05 ± 0.01	-0.28 ± 0.18	-0.21 ± 0.20	-0.12 ± 0.06	0.05 ± 0.15	1.13
J1545+2511	PS1	-0.16 ± 0.01	-0.14 ± 0.01	-0.16 ± 0.48	0.03 ± 0.52	-0.10 ± 0.04	0.14 ± 0.07	0.84
J1550+4139	DELS	-0.25 ± 0.01	-0.13 ± 0.02	-0.55 ± 0.49	-0.24 ± 0.57	-0.34 ± 0.06	0.12 ± 0.15	1.14
J1552+2737	PS1	0.03 ± 0.01	-0.26 ± 0.01	-0.45 ± 0.36	-0.37 ± 0.47	-0.25 ± 0.08	0.12 ± 0.17	0.89
J0126-0839	PS1	0.43 ± 0.01	0.15 ± 0.02	0.29 ± 0.18	0.25 ± 0.21	0.00 ± 0.09	0.00 ± 0.27	0.91
J0159+0033	DELS	0.28 ± 0.02	0.22 ± 0.02	1.15 ± 0.24	0.60 ± 0.28	0.12 ± 0.21	-0.01 ± 0.41	0.95
J1011+5442	PS1	1.04 ± 0.02	0.53 ± 0.02	1.91 ± 0.12	0.46 ± 0.15	1.30 ± 0.21	-0.50 ± 0.36	0.86
J1554+3629	DELS	-0.56 ± 0.01	-0.42 ± 0.02	-1.37 ± 0.39	-0.67 ± 0.49	-0.74 ± 0.08	0.16 ± 0.17	1.22
J2336+0017	DELS	0.41 ± 0.02	0.30 ± 0.02	0.41 ± 0.40	0.22 ± 0.45	0.14 ± 0.28	-0.17 ± 0.42	1.06

Note. Δg_{phot} and $\Delta(g-r)_{\text{phot}}$ are the g -band variability and $g-r$ color variability from imaging data, while Δg_{spec} and $\Delta(g-r)_{\text{spec}}$ are from spectrophotometry.

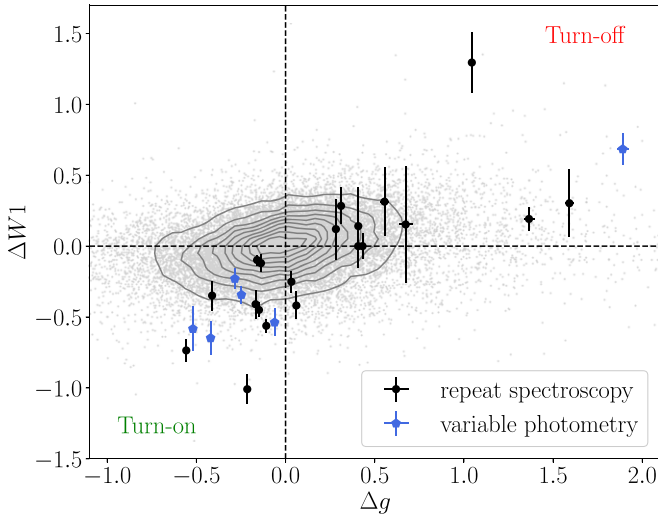


Figure 2. Variability of CL AGNs in the optical g -band and mid-infrared $W1$ band. The broadband fluxes in the optical and mid-infrared have the same trend. The CL AGNs marked as black dots are from repeat spectroscopy, and the blue pentagon shows CL AGNs selected from variable photometry. The region in the bottom left, where both the g - and $W1$ -bands brighten, is a region for turn-on CL AGN selection; the top right area, where both g and $W1$ are dimmed, is useful for turn-off CL AGN selection. The gray dots and the contours show quasars with a similar redshift range, $z < 0.7$.

calculated from propagation of SDSS g -band magnitude uncertainty and PS1 g -band magnitude uncertainty, or the DELS g -band magnitude uncertainty when available. Similarly, the $g-r$ color variation, $\Delta(g-r)$, is calculated by the color offset between PS1 $g-r$ color, or the DELS $g-r$ color when

available, and the SDSS $g-r$ color. The g -band variability ranges from -1.89 to 0.52 mag in this sample. As in some CL AGN cases, the PS1 or DELS images were taken before the type transition. We also calculate the spectrophotometry with the spectra convolved with the SDSS filters. The spectrophotometry are calibrated by setting the first epoch SDSS spectrophotometry equal to the SDSS photometry at the closest epoch. The variations of spectrophotometry in the g -band and $g-r$ color are also listed in Table 7. In the mid-infrared, there is a series of exposures within one day with a long interval of half a year in *WISE* multi-epoch data. We calculate the 3σ -clipped mean magnitude of *WISE* in $W1$ and $W2$ every half a year. The uncertainties of $W1$ and $W2$ are obtained from the 3σ -clipped standard deviation of $W1$ and $W2$ magnitude every half a year. There are less than 10 epochs of *WISE* mean magnitude for a single object. For the turn-on objects, the *WISE* variability is calculated from the offset between the brightest epoch photometry and the first epoch photometry. For turn-off objects, the *WISE* variability is calculated from the offset between the last epoch photometry and the brightest epoch photometry. The magnitude and color variability are calculated between the later epoch and the former epoch. Therefore, the magnitude variability is negative if an object becomes brighter, and the color variability is negative if the object becomes bluer. Figure 2 shows the optical broadband flux changes along with mid-infrared flux. In our sample, the mid-infrared variability $\Delta W1$ ranges from -1.01 to 0.68 , and 15 of them varied for more than 0.2 mag ($|\Delta W1| > 0.2$ mag). The mid-infrared flux is not significantly affected by dust extinction (Weingartner & Draine 2001). In the scenario of variable obscuration, the variation in the $W1$ band due to dust extinction yields a factor

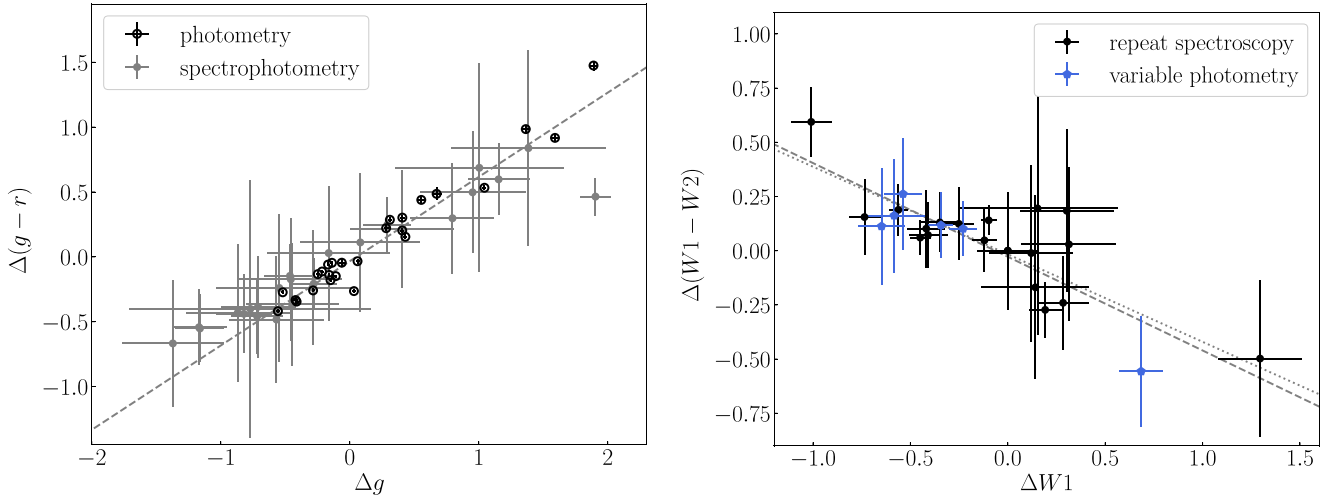


Figure 3. Color variability vs. magnitude variability of CL AGNs in the optical (left panel) and mid-infrared (right panel). A bluer-when-brighter chromatism is confirmed in the optical. However, the mid-infrared $W1-W2$ color is redder when brighter. The opposite color change trend in the mid-infrared is possibly due to a stronger contribution from the AGN dust torus when the AGN turns on.

of ~ 21 variability in g -band magnitude, according to the extinction curve in the optical and mid-infrared even considering micrometer-sized grains (Wang et al. 2015). A variability of 0.2 mag in the $W1$ band suggests approximately 4.2 mag variability in the g -band. The optical variability, from photometric and spectrophotometric data, is not consistent with the scenario of variable obscuration in 10 CL AGNs in our sample at more than the 3σ confidence level (J0831+3646, J0937+2602, J1003+3525, J1104+0118, J1110-0003, J1115+0544, J1132+0357, J1259+5515, J1447+2833, and J1550+4139) and in eight CL AGNs between the 1σ and 3σ confidence levels (J0849+2747, J1104+6343, J1150+3632, J1152+3209, J1319+6753, J1533+0110, J1545+2511, and J1552+2737). The accuracy of the spectrophotometry is lower than that of the photometry. Following-up with high-accuracy photometric data after the type transition can better constrain the mechanism of type transition. Using mid-infrared variability to select CL AGNs, we were inclined to select CL AGNs with intrinsic changes instead of varying obscuration.

5. Discussion

5.1. CL AGNs Color Variability

The optical and mid-infrared colors vary following flux changes. Figure 3 shows the color variability versus the magnitude variability in the optical (left panel) and mid-infrared (right panel). The bluer-when-brighter trend is a known trend in the optical (e.g., Wilhite et al. 2005; Schmidt et al. 2012; Zuo et al. 2012; Ruan et al. 2014). In the mid-infrared, there is a trend in which $W1-W2$ is redder when brighter. A similar $W1-W2$ color dependence on AGN luminosity is reported in the Swift/Burst Alert Telescope AGN sample (Ichikawa et al. 2017).

The global SED variation helps to clarify the color changes in the infrared. We construct the infrared SED using the *WISE* data and the near-infrared data from the Two Micron All Sky Survey (2MASS; Skrutskie et al. 2006), which scanned the entire sky from 1997 to 2001 in three bands: J ($1.25 \mu\text{m}$), H ($1.65 \mu\text{m}$), and K_s ($2.17 \mu\text{m}$). Because there are no multi-epoch near-infrared and *WISE* $W3$ and $W4$ data, we show examples of two different objects in Figure 4. The two objects are J1115

+0544 (left panel) at the faint state before it turned on and J0849+2747 (right panel) before it turned off.

We fit the SED with the stellar and dust torus emission components. The simple stellar synthesis model by Bruzual & Charlot (2003, hereafter BC03) with an age of 5 Gyr and solar metallicity is used for the stellar emission. The dust torus component is described by a new version of the radiative transfer model CAT3D (Hönl & Kishimoto 2017). Due to limitations of the data, we adopt the templates without the wind component. We perform the SED fitting with a new Markov chain Monte Carlo (MCMC) method (Shangguan et al. 2018) combining the stellar and dust torus models.

In the SED before the AGN turned on, the $W1$ and $W2$ bands generally follow the stellar emission. In the SED after the AGN turned on, the $W1$ and $W2$ bands, especially $W2$, were strongly affected by the dust torus radiation. Therefore, it is possible that the $W1-W2$ shows as blue without a strong AGN contribution, and turns out to be red after the AGN turning on. Thus the mid-infrared $W1-W2$ color of CL AGNs turns to be redder when brighter.

In the optical, the color-magnitude variation (dashed line in left panel in Figure 3) of CL AGNs (listed in Table 5) is fitted by a least-squares fitting algorithm as

$$\Delta(g-r) = (0.650 \pm 0.042)\Delta g - (0.034 \pm 0.017). \quad (1)$$

The CL AGNs selected from repeat spectroscopy are not biased by *WISE* variability selection criteria. For CL AGNs selected from repeat spectroscopy, the mid-infrared color-magnitude relation (dotted line in left panel in Figure 3) is fitted as

$$\begin{aligned} \Delta(W1-W2) \\ = (-0.404 \pm 0.078)\Delta W1 - (0.016 \pm 0.033). \end{aligned} \quad (2)$$

Thus, a selection criterion based on mid-infrared variability as $|\Delta(W1-W2)| > 0.1$ when $|\Delta W1| > 0.2$, is reasonable. With all the CL AGNs (in Table 5), the color-magnitude relation in the mid-infrared (dashed line in the left panel in Figure 3) is fitted as

$$\begin{aligned} \Delta(W1-W2) \\ = (-0.432 \pm 0.066)\Delta W1 - (0.028 \pm 0.028). \end{aligned} \quad (3)$$

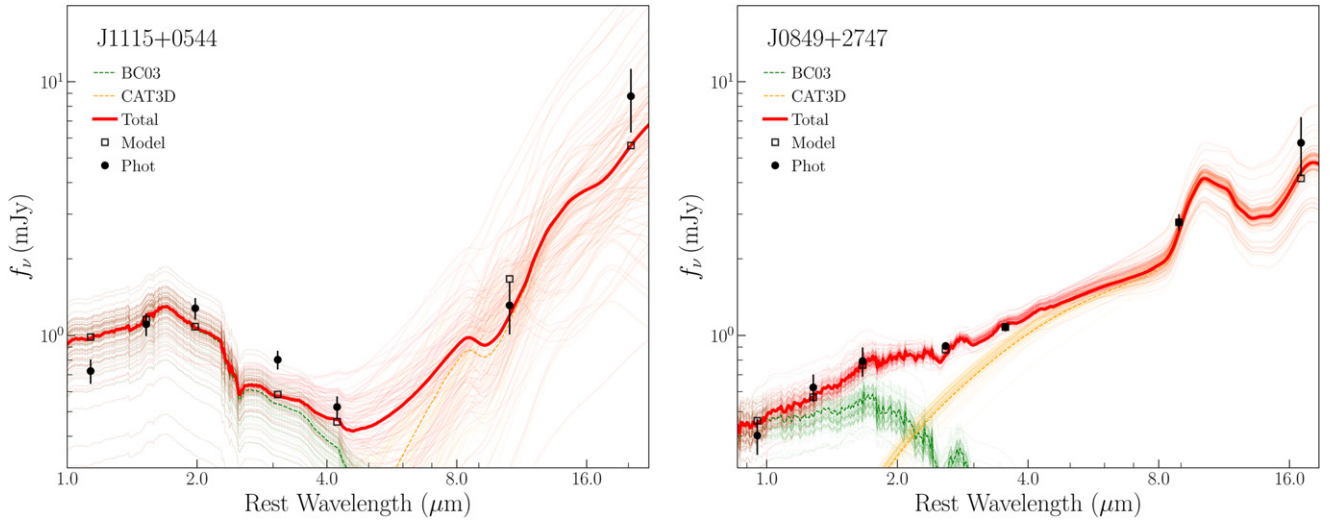


Figure 4. Infrared SED of two CL AGNs, J1115+0544 (left panel) and J0849+2747 (right panel). The green, red, and brown dashed lines are the BC03, CAT3D, and the combined models, while the light dotted lines are 100 random samples of the final model and each component from the MCMC method to demonstrate the uncertainty of the fitting. The black circles with error bars are the observed data (2MASS J , H , K_s , and $WISE$ $W1$, $W2$, $W3$, $W4$ data from short to long wavelengths). The empty squares are the modeled photometric data at the observed bands.

The CL AGNs, selected from *WISE* variability, obey the color-magnitude relation well. The mid-infrared variability and color variability are good tracers for CL AGNs with intrinsic changes.

5.2. The Timescale of the Type Transition

The current data coverage is not good enough to measure the timescale of transition. Therefore, we only roughly estimate the upper limit of type transition as follows. The upper limit of the transition timescale is obtained by the time interval between the former and recent spectroscopic epoch (Δt_{spec} in the rest-frame in Table 8). We further prescribe a limit to the timescale with the light curve changes approaching the transition. For example, although the two spectra of J1115+0544 were separated by 14 years, there was no variability detected in SDSS, PS1, and CRTS imaging data. The rapid flux brightening was detected by *WISE* in 2015. The $W1$ of J1115+0544 increased for more than 1 mag in a short interval, less than one year in the rest-frame. The light curves of CL AGNs keep quiescent at faint states, namely before the transition of turn-on CL AGNs or after the transition of turn-off CL AGNs. The CL AGNs usually vary in their AGN phase. In some cases (for example, J0831+3646, J1110-0003, J1115+0544, J1259+5515, and J1319+6753), the *WISE* flux increased when the AGN turned on, and decreased with a smaller amplitude later on, possibly due to the variability of the AGN accretion rate. On the other hand, it is also possible that the flux increase is due to the TDEs instead of AGN activity. In this scenario, the later light curve should continually decrease following the typical light curve of TDEs, which is proportional to $t^{-5/3}$ (Rees 1988; Lodato et al. 2009; Guillochon & Ramirez-Ruiz 2013). Follow-up photometric data are needed to distinguish the scenarios of AGN accretion rate variability and TDEs. The epoch approaching the type transition is obtained by a recent quiescent image epoch at the faint state, or the brightest image epoch in their AGN phase. In Table 8, Epoch1* and Epoch2* show the imaging data epochs (and imaging survey) approaching the transition before and after the type transition.

Δt , obtained from photometric variation approaching the type transition when available, is a better upper limit of the transition timescale in the rest-frame than Δt_{spec} . Therefore, the upper limit of the type transition timescales ranges from 0.9 to 12.6 years in the rest-frame.

The short transition timescale is not consistent with the scenario of variable obscuration (e.g., LaMassa et al. 2015; Gezari et al. 2017; Sheng et al. 2017). In a scenario of variable accretion rate, the CL timescale in this sample is much shorter than the inflow timescale of gas in the inner parts of the accretion disk, as discussed in previous works (LaMassa et al. 2015; MacLeod et al. 2016; Runnoe et al. 2016; Gezari et al. 2017). So modeling CL AGNs via changes in accretion rates is far from a settled matter. A detailed report on the mechanisms of the type transition will be presented in a subsequent paper.

6. Summary

We present surveys of CL AGNs in the SDSS spectra archive, the LAMOST spectra archive, and observations for some CL AGN candidates selected from photometric data. In total, we discover 21 new CL AGNs at $0.08 < z < 0.58$. Among the new CL AGNs, 5 were found by repeat spectra from the SDSS, 10 were discovered from repeat spectra in SDSS and LAMOST, and 6 were selected from photometric variability and confirmed by new spectroscopy. From our surveys, approximately 0.006% (0.007%) galaxies with repeat spectroscopy in the SDSS (SDSS and LAMOST) are CL AGNs, with obvious broad Balmer emission-line changes.

The physical mechanism of type transition is important for understanding the evolution of AGNs. The mid-infrared flux changes with the optical continuum flux. Variations of more than 0.2 mag in the mid-infrared were detected in 15 CL AGNs during the transition, and such variability suggests ~ 4.2 mag variability in the g -band. In the scenario of variable obscuration, the variation in the $W1$ band due to dust extinction yields a factor of ~ 21 variability in the g -band. The optical variability is not consistent with the scenario of variable obscuration in the

Table 8
Timescale of Changing-look AGN Transition

Name	Redshift	Epoch1	Epoch2	Δt_{spec} (years)	Epoch1*	Epoch2*	Δt (years)
J0831+3646	0.19501	52312	57367	11.6	PS1 56244	...	2.6
J0849+2747	0.29854	53350	56628	6.9	6.9
J0909+4747	0.11694	52620	57745	12.6	12.6
J0937+2602	0.16219	54524	57369	6.7	PS1 55845	...	3.6
J1003+3525	0.11886	53389	57867	11.0	PS1 55726	...	5.2
J1104+0118	0.57514	52374	57867	9.6	...	PS1 55902	6.1
J1104+6343	0.16427	52370	54498	5.0	5.0
J1110-0003	0.21922	51984	57864	13.2	...	WISE 57003	11.3
J1115+0544	0.08995	52326	57393	12.7	WISE 57002	WISE 57367	0.9
J1118+3203	0.3651	53431	56367	5.9	5.9
J1132+0357	0.09089	52642	57392	11.9	CRTS 56665	...	1.8
J1150+3632	0.34004	53436	57422	8.1	8.1
J1152+3209	0.37432	53446	57844	8.8	...	PS1 56063	5.2
J1259+5515	0.19865	52707	57863	11.8	WISE 55534	WISE 56806	2.9
J1319+6753	0.16643	51988	57867	13.8	...	WISE 56982	11.7
J1358+4934	0.11592	53438	54553	2.7	2.7
J1447+2833	0.16344	53764	57071	7.8	7.8
J1533+0110	0.14268	51989	54561	6.2	6.2
J1545+2511	0.11696	53846	57891	9.9	9.9
J1550+4139	0.22014	52468	57864	12.1	PS1 56233	...	3.7
J1552+2737	0.08648	53498	56722	8.1	PS1 55987	...	1.9

Note. Δg_{phot} and $\Delta(g - r)_{\text{phot}}$ are the g -band variability and $g - r$ color variability from imaging data, while Δg_{spec} and $\Delta(g - r)_{\text{spec}}$ are from spectrophotometry.

10 CL AGNs in our sample at more than the 3σ confidence level and in 8 CL AGNs between the 1σ and 3σ confidence levels. Follow-up high-accuracy photometric data after the type transition can better constrain the mechanism of the type transition.

The optical and mid-infrared colors change with flux variation. A bluer-when-brighter chromatism is confirmed in the optical bands. However, the mid-infrared $W1-W2$ color is redder when brighter. The opposite color change trend in the mid-infrared is possibly caused by a stronger contribution from the AGN dust torus when the AGNs turn on. The mid-infrared variability and colors are good tracers for CL AGNs with intrinsic variability.

The upper limit of type transition timescales ranges from 0.9 to 12.6 years in the rest-frame. The mid-infrared emission of J1115+0544 increased for more than 1 mag in a short interval, less than one year in the rest-frame. The timescale of the type transition will help distinguish the mechanism of the changes. Follow-up photometric data are needed to distinguish the scenarios of AGN accretion rate variability and TDEs based on the decreasing light curve trend of TDEs ($\sim t^{-5/3}$).

The photometric variability of CL AGNs provides ways to select CL AGNs from large-area surveys. In the future, the Large Synoptic Survey Telescope (LSST; Ivezić et al. 2008), with multi-epoch and multi-band data, will provide powerful data for CL AGN selection and monitoring.

In future papers we will analyze the spectra and imaging data in more detail, and discuss their probable transition mechanism. The rareness of CL AGNs provides exceptional opportunities studies of the $M-\sigma_*$ relation at higher redshift with faint-state spectra and AGN-phase spectra. We plan to estimate their black hole masses from the $M-\sigma_*$ relation, and compare with their virial black hole masses obtained from the single-epoch spectra. The images of CL AGNs at faint states are useful for studies of AGN host galaxies and help to avoid contamination

from the luminous central engines. We will perform a statistical study on the host galaxy properties of CL AGNs.

The work is supported by the National Key R&D Program of China (2016YFA0400703), National Key Basic Research Program of China 2014CB845700, the NSFC grant No.11373008 and No.11533001. We thank Luis Ho, Yue Shen, Arjun Dey, Nicholas Ross, Aaron Meisner, and Ning Jiang, Yanxia Xie for very helpful discussions. We thank Shu Wang for providing the extinction data.

We acknowledge the use of SDSS data. Funding for SDSS-III has been provided by the Alfred P. Sloan Foundation, the Participating Institutions, the National Science Foundation, and the U.S. Department of Energy Office of Science. The SDSS-III website is <http://www.sdss3.org/>. SDSS-III is managed by the Astrophysical Research Consortium for the Participating Institutions of the SDSS-III Collaboration including the University of Arizona, the Brazilian Participation Group, Brookhaven National Laboratory, Carnegie Mellon University, University of Florida, the French Participation Group, the German Participation Group, Harvard University, the Instituto de Astrofísica de Canarias, the Michigan State/Notre Dame/JINA Participation Group, Johns Hopkins University, Lawrence Berkeley National Laboratory, Max Planck Institute for Astrophysics, Max Planck Institute for Extraterrestrial Physics, New Mexico State University, New York University, Ohio State University, Pennsylvania State University, University of Portsmouth, Princeton University, the Spanish Participation Group, University of Tokyo, University of Utah, Vanderbilt University, University of Virginia, University of Washington, and Yale University.

We acknowledge the use of LAMOST data. The Large Sky Area Multi-Object Fiber Spectroscopic Telescope (LAMOST, also named Guoshoujing Telescope) is a National Major Scientific Project built by the Chinese Academy of Sciences. Funding for the project has been provided by the National

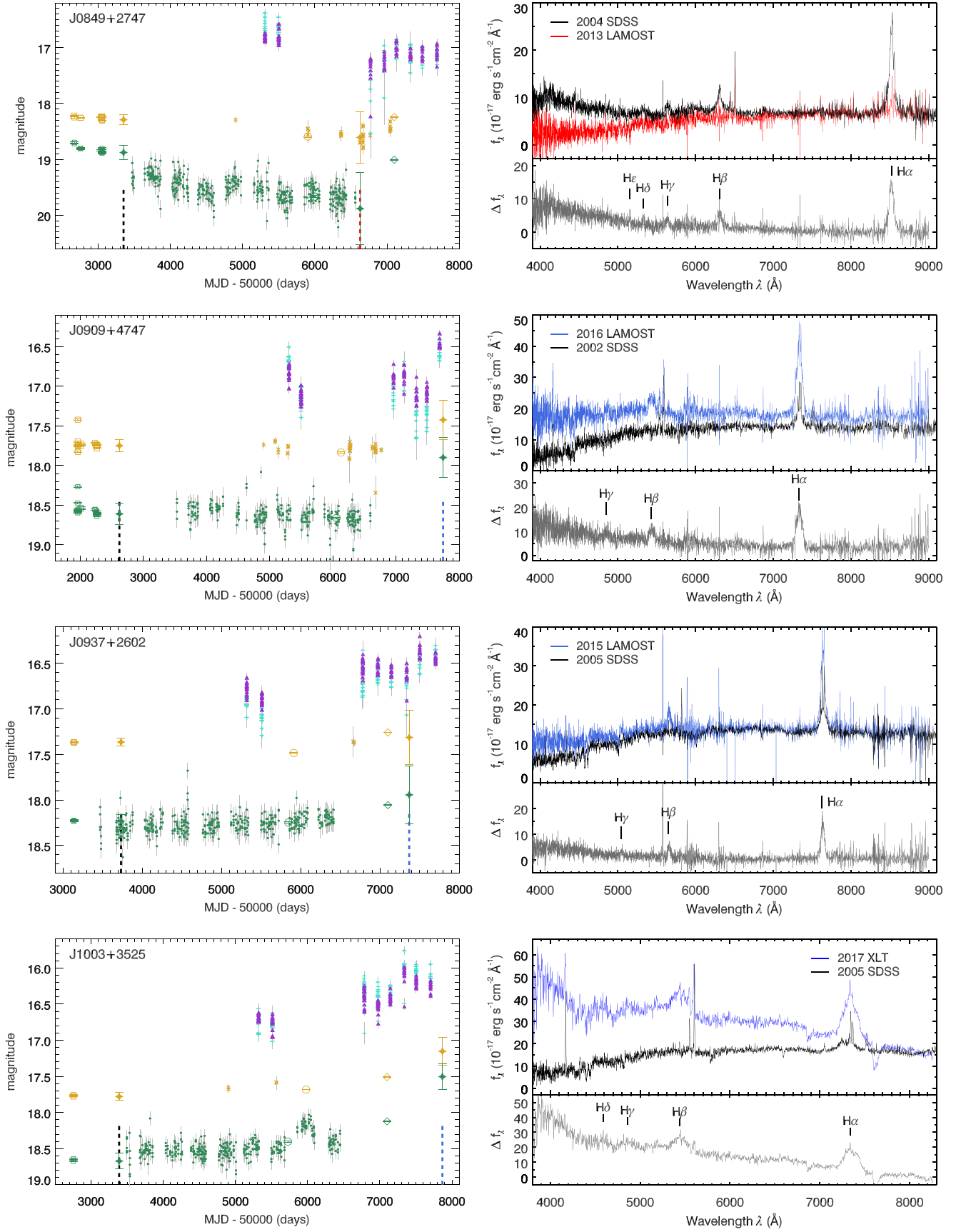


Figure 5. Same as Figure 1.

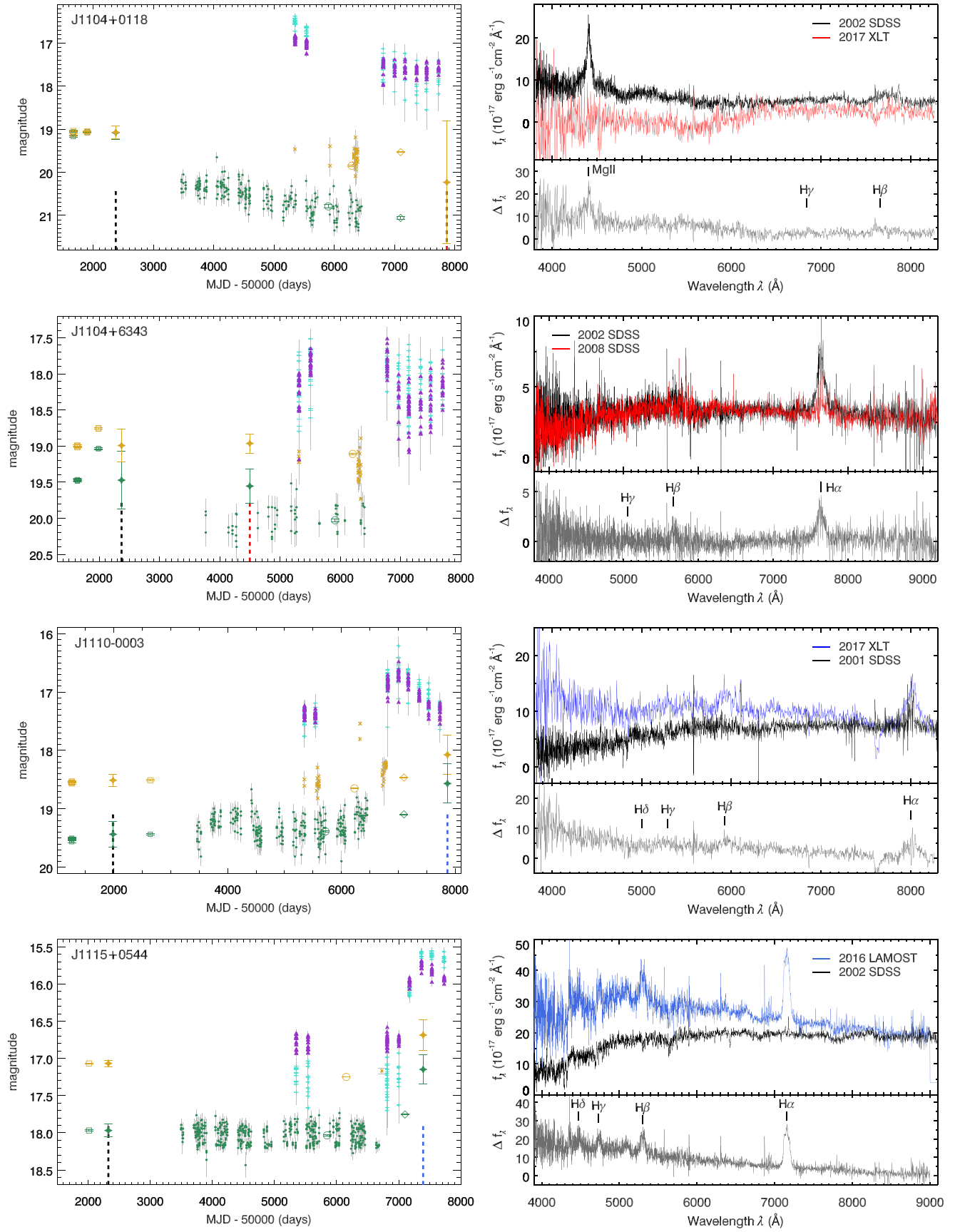


Figure 5. (Continued.)

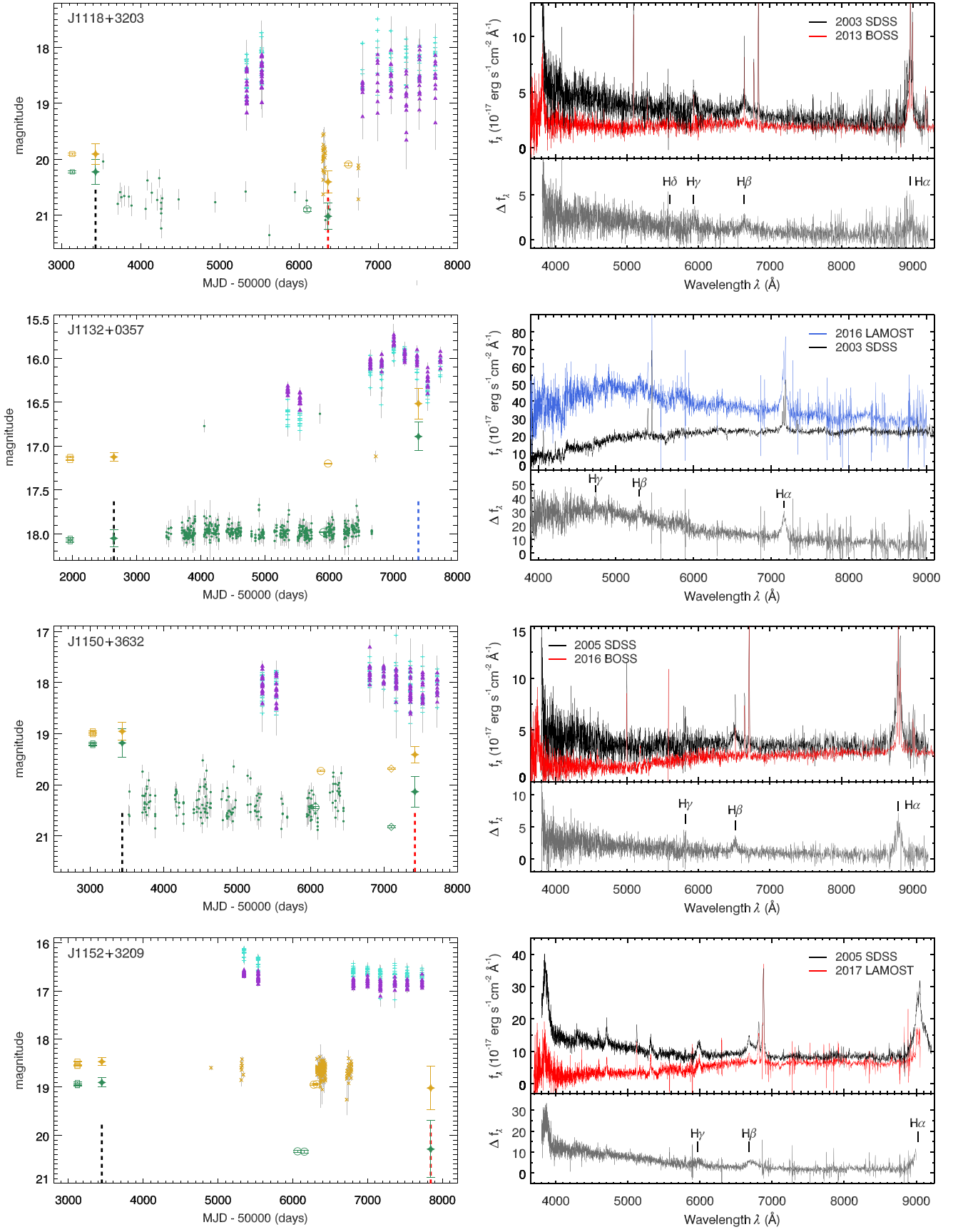


Figure 5. (Continued.)

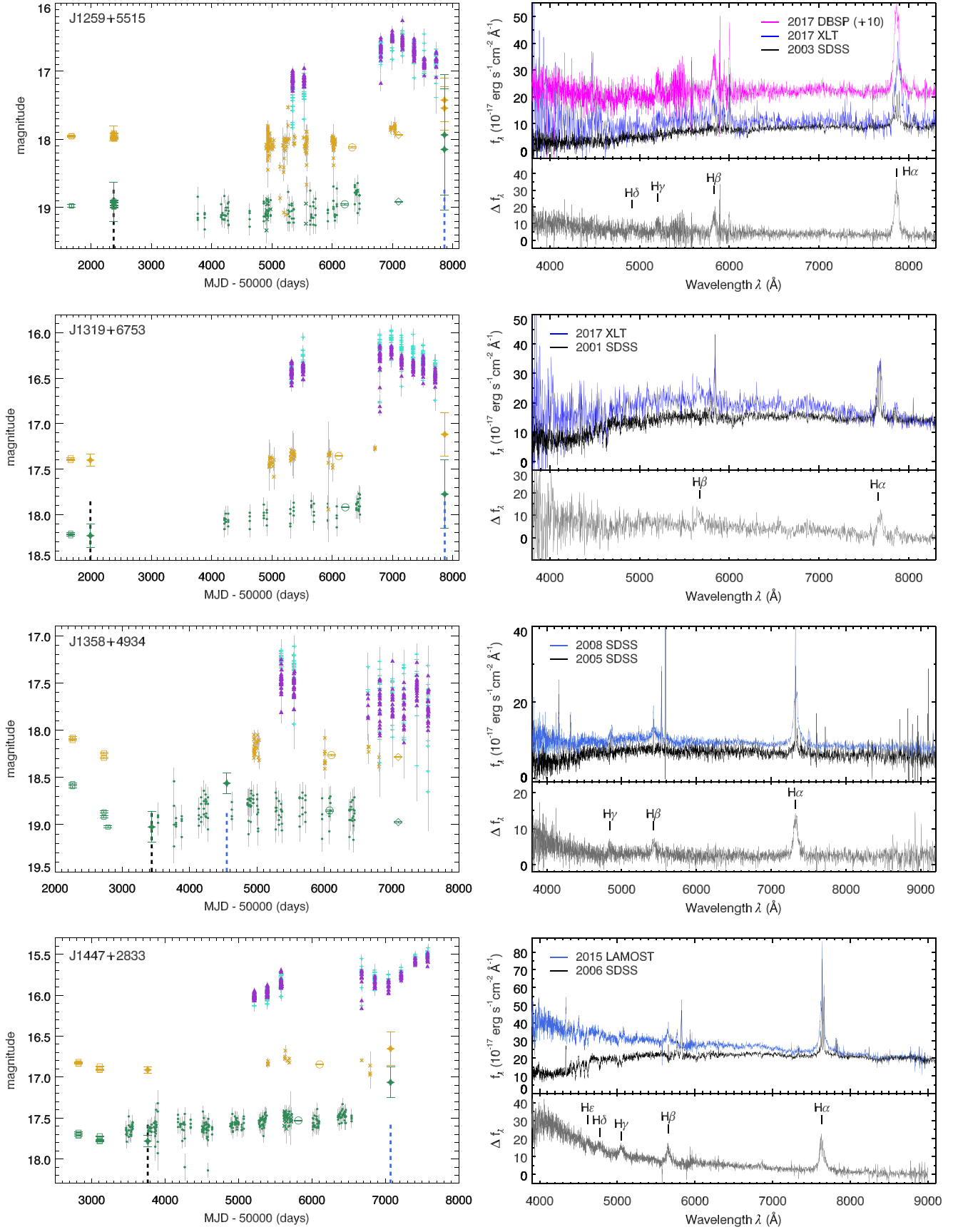


Figure 5. (Continued.)

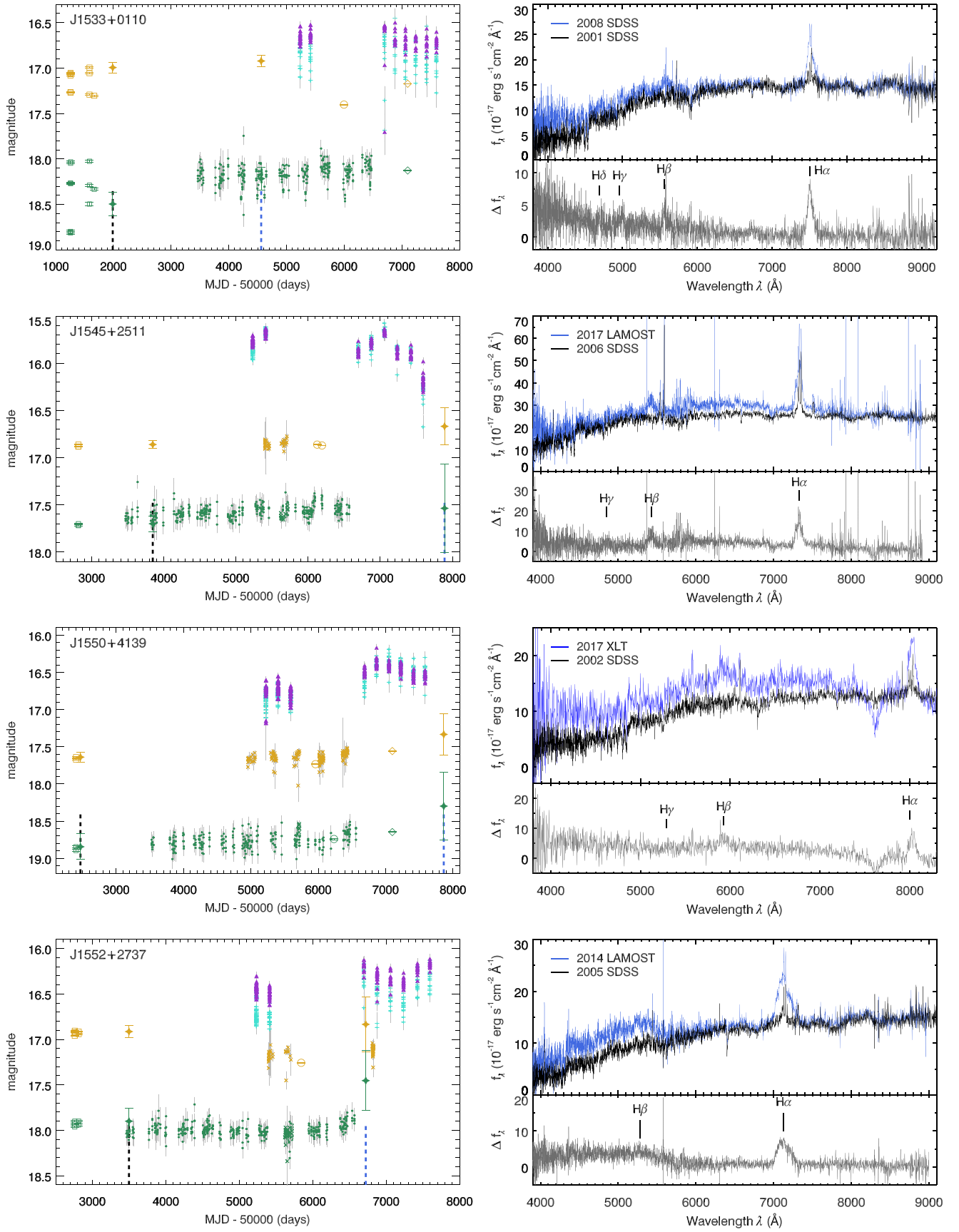


Figure 5. (Continued.)

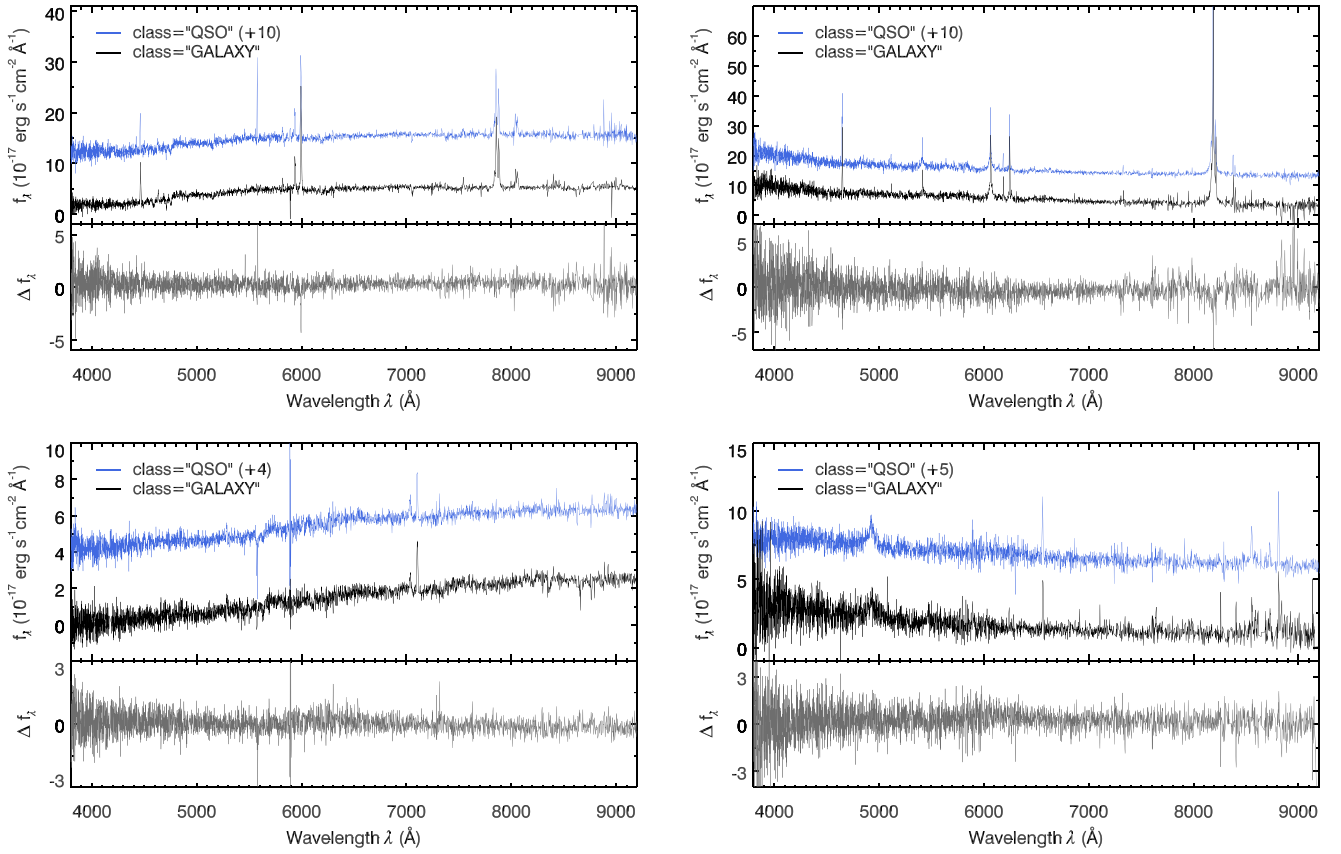


Figure 6. Four CL candidates in the SDSS that were rejected by visual inspection. From low to high redshift, the four objects are J0001–0005 (left upper panel), J1356–0115 (right upper panel), J0803+4258 (left bottom panel), and J0937+3232 (right bottom panel). To show the spectra at different epochs, a constant is added to the spectra that were classified as “QSO.”

Development and Reform Commission. LAMOST is operated and managed by the National Astronomical Observatories, Chinese Academy of Sciences.

This research has made use of PS1, DELS, *WISE*, CRTS, and PTF imaging data. The PS1 has been made possible through contributions by the Institute for Astronomy, the University of Hawaii, the Pan-STARRS Project Office, the Max-Planck Society and its participating institutes, the Max Planck Institute for Astronomy, Heidelberg and the Max Planck Institute for Extraterrestrial Physics, Garching, The Johns Hopkins University, Durham University, the University of Edinburgh, Queen’s University Belfast, the Harvard-Smithsonian Center for Astrophysics, the Las Cumbres Observatory Global Telescope Network Incorporated, the National Central University of Taiwan, the Space Telescope Science Institute, the National Aeronautics and Space Administration under grant No. NNX08AR22G issued through the Planetary Science Division of the NASA Science Mission Directorate, the National Science Foundation under grant No. AST-1238877, the University of Maryland, and Eotvos Lorand University (ELTE). We acknowledge the use of the DESI Legacy imaging survey, whose website is <http://legacysurvey.org>. This research has made use of the NASA/ IPAC Infrared Science Archive, which is operated by the Jet Propulsion Laboratory, California Institute of Technology, under contract with the National Aeronautics and Space Administration. This publication makes use of data products from the *Wide-field Infrared Survey Explorer*, which is a joint project of the University of California, Los Angeles, and the Jet Propulsion

Laboratory/California Institute of Technology, funded by the National Aeronautics and Space Administration. The CSS survey is funded by the National Aeronautics and Space Administration under grant No. NNG05GF22G issued through the Science Mission Directorate Near-Earth Objects Observations Programme. The CRTS survey is supported by the US National Science Foundation under grants AST-0909182 and AST-1313422. We acknowledge the use of PTF data; the PTF website is <https://www.ptf.caltech.edu>.

We acknowledge the use of the Xinglong 2.16 m telescope and the Palomar Hale 5 m telescope. This work has made use of the TOPCAT (Taylor 2005). We thank the Chinese Virtual Observatory; its website is <http://www.china-vo.org>.

Facilities: Sloan, PS1, IRSA, *WISE*, Beijing:2.16 m (BFOSC), Palomar P200/Caltech.

Appendix

The light curves and spectra of the other 20 new CL AGNs, in addition to the CL AGN shown in Figure 1, are provided in Figure 5.

Figure 6 shows some examples of CL candidates in the SDSS rejected by our visual inspection. Table 9 summarizes some details about the four CL candidates. They were classified as “QSO” and “GALAXY” at different epochs in the SDSS. As shown in the residual spectra, there is no dramatic change. As the SDSS spectroscopic pipelines classify the objects through a comparison of individual spectra with galaxy, QSO, and stellar templates, these objects were classified as

Table 9
Examples of CL Candidates Rejected by Visual Inspection in the SDSS

Name	R.A.	Decl.	Redshift	Epoch(GALAXY)	Epoch(QSO)
J0001−0005	00:01:07.52	−00:05:52.3	0.19754	55477	52943
J1356−0115	13:56:18.49	−01:15:14.0	0.24726	51942	52721
J0803+4258	08:03:47.55	+42:58:38.9	0.41881	55245	55178
J0937+3232	09:37:35.46	+32:32:49.9	0.76017	54807	56310

Note. Epoch(GALAXY) and Epoch(QSO) describe the MJDs of the spectra that were classified as “GALAXY” and “QSO,” respectively.

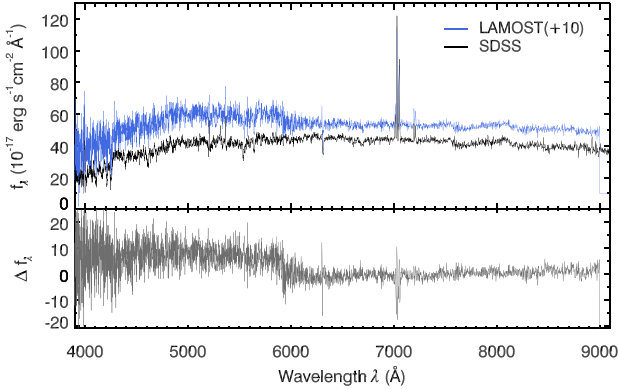


Figure 7. Example of CL candidates in SDSS and LAMOST that were rejected by visual inspection.

different types possibly due to marginally different spectral S/Ns at different epochs.

The spectra were classified by the LAMOST 1D pipeline into four primary classifications, namely “STAR,” “GALAXY,” “QSO,” and “UNKNOWN,” through matching individual spectra with templates (Luo et al. 2015). Among the 8171 objects, approximately 36% of them are classified as “UNKNOWN” and 7% are classified as “STAR.” The S/N of objects classified as “UNKNOWN” is low due to unstable fiber efficiency, non-photometric observational conditions, or they are too faint for the LAMOST survey (Ai et al. 2016). None of the 10 CL AGNs from LAMOST were classified as “UNKNOWN” or “STAR.” Figure 7 shows an example of CL candidates in the SDSS and LAMOST that were rejected by visual inspection. There is a break around 5700–5900 Å in the LAMOST spectrum due to inappropriate combination of the spectra in the blue and red arms, resulting in flux intensity variation in the automatic program check process.

ORCID iDs

Qian Yang <https://orcid.org/0000-0002-6893-3742>
 Xue-Bing Wu <https://orcid.org/0000-0002-7350-6913>
 Xiaohui Fan <https://orcid.org/0000-0003-3310-0131>
 Linhua Jiang <https://orcid.org/0000-0003-4176-6486>
 Ian McGreer <https://orcid.org/0000-0002-3461-5228>
 Jinyi Shanguan <https://orcid.org/0000-0002-4569-9009>
 Feige Wang <https://orcid.org/0000-0002-7633-431X>
 Jinyi Yang <https://orcid.org/0000-0001-5287-4242>

References

Abazajian, K. N., Adelman-McCarthy, J. K., Agüeros, M. A., et al. 2009, *ApJS*, 182, 543
 Abolfathi, B., Aguado, D. S., Aguilar, G., et al. 2017, arXiv:1707.09322
 Ai, Y. L., Wu, X.-B., Yang, J., et al. 2016, *AJ*, 151, 24

Antonucci, R. 1993, *ARA&A*, 31, 473
 Antonucci, R. R. J., & Cohen, R. D. 1983, *ApJ*, 271, 564
 Antonucci, R. R. J., & Miller, J. S. 1985, *ApJ*, 297, 621
 Ballo, L., Giustini, M., Schartel, N., et al. 2008, *A&A*, 483, 137
 Bianchi, S., Guainazzi, M., Matt, G., et al. 2005, *A&A*, 442, 185
 Blanchard, P. K., Nicholl, M., Berger, E., et al. 2017, *ApJ*, 843, 106
 Bolton, A. S., Schlegel, D. J., Aubourg, E., et al. 2012, *AJ*, 144, 144
 Bruzual, G., & Charlot, S. 2003, *MNRAS*, 344, 1000
 Calderone, G., Nicastro, L., Ghisellini, G., et al. 2017, *MNRAS*, 472, 4051
 Chambers, K. C., Magnier, E. A., Metcalfe, N., et al. 2016, arXiv:1612.05560
 Cohen, R. D., Puetter, R. C., Rudy, R. J., Ake, T. B., & Foltz, C. B. 1986, *ApJ*, 311, 135
 Cui, X.-Q., Zhao, Y.-H., Chu, Y.-Q., et al. 2012, *RAA*, 12, 1197
 Dawson, K. S., Schlegel, D. J., Ahn, C. P., et al. 2013, *AJ*, 145, 10
 Denney, K. D., De Rosa, G., Croxall, K., et al. 2014, *ApJ*, 796, 134
 Dey, A., Schlegel, D. J., Lang, D., et al. 2018, *AJ*, submitted (arXiv:1804.08657)
 Drake, A. J., Djorgovski, S. G., Mahabal, A., et al. 2009, *ApJ*, 696, 870
 Du, B., Luo, A.-L., Kong, X., et al. 2016, *ApJS*, 227, 27
 Eisenstein, D. J., Weinberg, D. H., Agol, E., et al. 2011, *AJ*, 142, 72
 Elitzur, M. 2012, *ApJL*, 747, L33
 Elitzur, M., Ho, L. C., & Trump, J. R. 2014, *MNRAS*, 438, 3340
 Eracleous, M., Livio, M., Halpern, J. P., & Storchi-Bergmann, T. 1995, *ApJ*, 438, 610
 Fan, Z., Wang, H., Jiang, X., et al. 2016, *PASP*, 128, 115005
 Flaugher, B. 2005, *JMPA*, 20, 3121
 Fukugita, M., Ichikawa, T., Gunn, J. E., et al. 1996, *AJ*, 111, 1748
 Gezari, S., Hung, T., Cenko, S. B., et al. 2017, *ApJ*, 835, 144
 Guillochon, J., & Ramirez-Ruiz, E. 2013, *ApJ*, 767, 25
 Gunn, J. E., Siegmund, W. A., Mannery, E. J., et al. 2006, *AJ*, 131, 2332
 He, B., Fan, D., Cui, C., et al. 2016, arXiv:1601.02334
 Hönig, S. F., & Kishimoto, M. 2017, *ApJL*, 838, L20
 Hutchinson, T. A., Bolton, A. S., Dawson, K. S., et al. 2016, *AJ*, 152, 205
 Hutsemekers, D., Agís González, B., Sluse, D., Ramos Almeida, C., & Acosta Pulido, J.-A. 2017, *A&A*, 604, L3
 Ichikawa, K., Ricci, C., Ueda, Y., et al. 2017, *ApJ*, 835, 74
 Ivezić, Z., Tyson, J. A., Abel, B., et al. 2008, arXiv:0805.2366
 Khachikian, E. Y., & Weedman, D. W. 1971, *ApJL*, 164, L109
 Korista, K. T., & Goad, M. R. 2004, *ApJ*, 606, 749
 Kormendy, J., & Ho, L. C. 2013, *ARA&A*, 51, 511
 LaMassa, S. M., Cales, S., Moran, E. C., et al. 2015, *ApJ*, 800, 144
 Law, N. M., Kulkarni, S. R., Dekany, R. G., et al. 2009, *PASP*, 121, 1395
 Lodato, G., King, A. R., & Pringle, J. E. 2009, *MNRAS*, 392, 332
 Luo, A.-L., Zhang, H.-T., Zhao, Y.-H., et al. 2012, *RAA*, 12, 1243
 Luo, A.-L., Zhao, Y.-H., Zhao, G., et al. 2015, *RAA*, 15, 1095
 Lyutyj, V. M., Oknyanskij, V. L., & Chuvayev, K. K. 1984, *SvAL*, 10, 335
 MacLeod, C. L., Ross, N. P., Lawrence, A., et al. 2016, *MNRAS*, 457, 389
 MacLeod, C. L., Ivezić, Ž., Sesar, B., et al. 2012, *ApJ*, 753, 106
 Mainzer, A., Bauer, J., Cutri, R. M., et al. 2014, *ApJ*, 792, 30
 Mainzer, A., Grav, T., Bauer, J., et al. 2011, *ApJ*, 743, 156
 Marchese, E., Braito, V., Della Ceca, R., Caccianiga, A., & Severgnini, P. 2012, *MNRAS*, 421, 1803
 Marin, F. 2017, *A&A*, 607, A40
 Martini, P., & Schneider, D. P. 2003, *ApJL*, 597, L109
 Matt, G., Guainazzi, M., & Maiolino, R. 2003, *MNRAS*, 342, 422
 McElroy, R. E., Husemann, B., Croom, S. M., et al. 2016, *A&A*, 593, L8
 Merloni, A., Dwelly, T., Salvato, M., et al. 2015, *MNRAS*, 452, 69
 Moran, E. C., Halpern, J. P., & Helfand, D. J. 1996, *ApJS*, 106, 341
 Nenkova, M., Sirocky, M. M., Ivezić, Ž., & Elitzur, M. 2008a, *ApJ*, 685, 147
 Nenkova, M., Sirocky, M. M., Nikutta, R., Ivezić, Ž., & Elitzur, M. 2008b, *ApJ*, 685, 160
 Netzer, H. 2015, *ARA&A*, 53, 365
 Osterbrock, D. E. 1977, *ApJ*, 215, 733
 Osterbrock, D. E. 1981, *ApJ*, 249, 462
 Osterbrock, D. E., & Koski, A. T. 1976, *MNRAS*, 176, 61P

- Pâris, I., Petitjean, P., Ross, N. P., et al. 2017, *A&A*, **597**, A79
- Penston, M. V., & Perez, E. 1984, *MNRAS*, **211**, 33P
- Piconcelli, E., Fiore, F., Nicastro, F., et al. 2007, *A&A*, **473**, 85
- Rees, M. J. 1988, *Natur*, **333**, 523
- Ricci, C., Bauer, F. E., Arevalo, P., et al. 2016, *ApJ*, **820**, 5
- Risaliti, G., Miniutti, G., Elvis, M., et al. 2009, *ApJ*, **696**, 160
- Ruan, J. J., Anderson, S. F., Cales, S. L., et al. 2016, *ApJ*, **826**, 188
- Ruan, J. J., Anderson, S. F., Dexter, J., & Agol, E. 2014, *ApJ*, **783**, 105
- Rumbaugh, N., Shen, Y., Morganson, E., et al. 2018, *ApJ*, **854**, 160
- Runnoe, J. C., Cales, S., Ruan, J. J., et al. 2016, *MNRAS*, **455**, 1691
- Schmidt, K. B., Rix, H.-W., Shields, J. C., et al. 2012, *ApJ*, **744**, 147
- Schneider, D. P., Richards, G. T., Hall, P. B., et al. 2010, *AJ*, **139**, 2360
- Seyfert, C. K. 1943, *ApJ*, **97**, 28
- Shangguan, J., Ho, L. C., & Xie, Y. 2018, *ApJ*, **854**, 158
- Shapovalova, A. I., Popović, L. Č., Burenkov, A. N., et al. 2010, *A&A*, **509**, A106
- Shappee, B. J., Prieto, J. L., Grupe, D., et al. 2014, *ApJ*, **788**, 48
- Sheng, Z., Wang, T., Jiang, N., et al. 2017, *ApJL*, **846**, L7
- Skrutskie, M. F., Cutri, R. M., Stiening, R., et al. 2006, *AJ*, **131**, 1163
- Smee, S. A., Gunn, J. E., Uomoto, A., et al. 2013, *AJ*, **146**, 32
- Stern, J., & Laor, A. 2012, *MNRAS*, **426**, 2703
- Stoughton, C., Lupton, R. H., Bernardi, M., et al. 2002, *AJ*, **123**, 485
- Taylor, M. B. 2005, in ASP Conf. Ser. 347, Astronomical Data Analysis Software and Systems XIV, ed. P. Shopbell, M. Britton, & R. Ebert (San Francisco, CA: ASP), 29
- Tody, D. 1986, *Proc. SPIE*, **627**, 733
- Tody, D. 1993, in ASP Conf. Ser. 52, Astronomical Data Analysis Software and Systems II, ed. R. J. Hanisch, R. J. V. Brissenden, & J. Barnes (San Francisco, CA: ASP), 173
- Urry, C. M., & Padovani, P. 1995, *PASP*, **107**, 803
- Vanden Berk, D. E., Richards, G. T., Bauer, A., et al. 2001, *AJ*, **122**, 549
- Vanden Berk, D. E., Wilhite, B. C., Kron, R. G., et al. 2004, *ApJ*, **601**, 692
- Wang, J.-M., & Zhang, E.-P. 2007, *ApJ*, **660**, 1072
- Wang, S., Li, A., & Jiang, B. W. 2015, *MNRAS*, **454**, 569
- Weingartner, J. C., & Draine, B. T. 2001, *ApJ*, **548**, 296
- Wilhite, B. C., Vanden Berk, D. E., Kron, R. G., et al. 2005, *ApJ*, **633**, 638
- Wright, E. L., Eisenhardt, P. R. M., Mainzer, A. K., et al. 2010, *AJ*, **140**, 1868
- Wu, X.-B., Zhang, W., & Zhou, X. 2004, *ChJAA*, **4**, 17
- Yang, Q., Wu, X.-B., Fan, X., et al. 2017, *AJ*, **154**, 269
- Zhao, G., Zhao, Y.-H., Chu, Y.-Q., Jing, Y.-P., & Deng, L.-C. 2012, *RAA*, **12**, 723
- Zou, H., Zhang, T., Zhou, Z., et al. 2017, *AJ*, **153**, 276
- Zuo, W., Wu, X.-B., Liu, Y.-Q., & Jiao, C.-L. 2012, *ApJ*, **758**, 104